

Annual Review of Fluid Mechanics

Elastocapillarity: When Surface Tension Deforms Elastic Solids

José Bico, Étienne Reyssat, and Benoît Roman

Physique et Mécanique des Milieux Hétérogènes, ESPCI-Paris, PSL Research University, CNRS, Sorbonne Université, and Université Paris Diderot, 75005 Paris, France; email: jose.bico@espci.fr, etienne.reyssat@espci.fr, benoit.roman@espci.fr

Annu. Rev. Fluid Mech. 2018. 50:629–59

First published as a Review in Advance on October 23, 2017

The *Annual Review of Fluid Mechanics* is online at fluid.annualreviews.org<https://doi.org/10.1146/annurev-fluid-122316-050130>Copyright © 2018 by Annual Reviews.
All rights reserved**ANNUAL REVIEWS Further**

Click here to view this article's online features:

- Download figures as PPT slides
- Navigate linked references
- Download citations
- Explore related articles
- Search keywords

Keywords

capillarity, elasticity, interfacial flows, fluid–structure interaction

Abstract

Although negligible at large scales, capillary forces may become dominant for submillimetric objects. Surface tension is usually associated with the spherical shape of small droplets and bubbles, wetting phenomena, imbibition, or the motion of insects at the surface of water. However, beyond liquid interfaces, capillary forces can also deform solid bodies in their bulk, as observed in recent experiments with very soft gels. Capillary interactions, which are responsible for the cohesion of sandcastles, can also bend slender structures and induce the bundling of arrays of fibers. Thin sheets can spontaneously wrap liquid droplets within the limit of the constraints dictated by differential geometry. This review aims to describe the different scaling parameters and characteristic lengths involved in elastocapillarity. We focus on three main configurations, each characterized by a specific dimension: three-dimensional (3D), deformations induced in bulk solids; 1D, bending and bundling of rod-like structures; and 2D, bending and stretching of thin sheets. Although each configuration deserves a detailed review, we hope our broad description provides a general view of elastocapillarity.

1. INTRODUCTION

Capillary length:

$$\ell_c = \sqrt{\frac{\gamma}{\rho g}}$$

Fluid–structure interactions are traditionally considered at large scales: Wind dynamic pressure blows up the sails of a ship, whereas hydrostatic pressure tends to deform the hull. Rain may complicate maneuvering on the deck, but the capillary forces responsible for the spherical shape of the droplets have a negligible impact at this scale. At small scales (more precisely, at small Reynolds numbers), interactions between viscous forces and soft structures are important in the locomotion of microorganisms and can induce deformations of cells or blood vessels, as recently reviewed by Duprat & Stone (2015). It is well known that surface tension forces are associated with the motion of aquatic insects on the surface of water, capillary rise, and wetting (de Gennes et al. 2004). In terms of length scale, capillarity becomes dominant over gravity below the capillary length, $\ell_c = \sqrt{\gamma/\rho g}$. Beyond liquid interfaces, can surface tension (or surface stress) also deform solids?

Recent technological advances in microfabrication and the development of very soft materials have motivated numerous studies of the coupling between surface tension and elasticity. In this review, we explore the currently blooming field of elastocapillarity. We develop three main configurations, each characterized by a specific dimension. In three dimensions, at which scale may surface tension deform bulk solids? In one dimension, how do bundles spontaneously appear in a brush removed from a liquid bath? In two dimensions, can a thin sheet spontaneously wrap a droplet?

This review does not pretend to be exhaustive, and interested readers are invited to read other, more specific reviews as a complement to this one. A recent review by Style et al. (2017) presents the most recent advances in the deformation of a bulk solid by surface tension. Snoeijer (2016) also discusses the coupling of lubrication flow, surface tension, and elasticity with the illustration of the familiar scraper coating process. Many reviews have been dedicated to the self-assembly of small objects by capillary forces (Boncheva & Whitesides 2005, Mastrangeli et al. 2009) and to the collapse (Maboudian 1997) or folding (Syms et al. 2003, Leong et al. 2010, Crane et al. 2013) of engineered microstructures. In surface engineering, researchers have made impressive achievements with arrays of nanorods or carbon nanotubes assembled through capillary interactions (De Volder & Hart 2013, Tawfick et al. 2016). Recent reviews have described the bundling of arrays of fibers from an academic perspective (Roman & Bico 2010, Duprat & Stone 2015).

The present review aims to provide a broad overview of elastocapillarity. The description of each configuration is limited to main scaling laws, with the hope that they bring useful physical insights. More specific details are provided by the references in the Literature Cited.

2. CAPILLARITY AND BULK ELASTICITY

2.1. The Elastocapillary Length

Surface tension is mostly thought to be of interest for liquids. However, solids are also subject to interfacial stresses that may induce deformations. Nevertheless, a key difference between simple liquids and solids is the ability of solid interfaces to sustain finite strains. Consequently, surface stresses in solids are, in principle, strain dependent. The surface stress Υ and surface energy γ of a solid are related through the Shuttleworth equation, which in its simplest form reads

$$\Upsilon = \gamma + \frac{d\gamma}{d\varepsilon}, \quad 1.$$

where ε is the interfacial strain (Andreotti & Snoeijer 2016).

On which scale may surface stresses induce deformations in elastic solids? While trying to measure the surface tension of solids (metals or ionic crystals), Nicolson (1955) has shown that the characteristic length scale at which surface stresses become important is defined by the competition

between surface forces and bulk elastic stresses. The characteristic stress resulting from surface tension, given by the classical Laplace law, is of order Υ/L , where L is the size of the solid sample. Such stresses may induce elastic deformations in the bulk of the solid. The induced strain becomes of order one when stresses reach the shear modulus G of the solid. The effect of surface stresses is thus important on structures whose characteristic size is smaller than the shear elastocapillary length:

$$\ell_S = \Upsilon/G. \quad 2.$$

Shear elastocapillary length: $\ell_S = \Upsilon/G$

For ordinary materials such as glass, the surface tension is of order 250 mN/m, for an elastic modulus $G \simeq 20$ GPa, so that $\ell_S \sim 10$ pm is below atomic scales. Similarly, in the case of copper, Υ and G are approximately 1.8 N/m and 50 GPa, respectively, and we obtain $\ell_S \sim 40$ pm. For such hard solids, precise X-ray measurements may detect small variations in the lattice parameter as a function of the size of the sample, but for most purposes, surface effects remain undetected. In the past decade, there has been a lot of interest in much softer materials such as elastomers, gels, or biological tissues. These materials are highly compliant, with typical G values of 0.1–1,000 kPa and Υ values of 0.01–0.1 N/m. For this class of materials, ℓ_S is at least 10 nm and may be as large as 1 mm. Such deformations may provide ways to measure the surface tension of a solid–fluid interface, which remains poorly documented. Capillary-induced deformations also constitute a useful tool to probe the mechanics of biological cells, as recently reported by Campàs et al. (2013).

2.1.1. Softening sharp solids. As in the case for liquid–gas interfaces, the surface tension of solids tends to smooth interfaces with high curvatures. For instance, several experimental and theoretical studies motivated by contact printing discuss the rounding off of the sharp edges of printing stamps made of soft elastomeric materials (Hui et al. 2002). These stamps are initially formed into a stiff mold. When peeled off the master copy, the topography of the replica tends to be smoothed out by surface stresses. For instance, a corner initially at a right angle is rounded off with a radius $R \sim \Upsilon/G$ (**Figure 1a**). Similarly, Mora et al. (2013) reported the softening by surface tension of the edges of a prism made of a very soft gel ($G \sim 50$ kPa) (**Figure 1b**). Mora & Pomeau (2015) also analytically derive the shape of angular solids in the asymptotic regimes of very shallow or extremely sharp wedges. The softening of the edges of a solid also induces more global deformations at the large scale of a slender object, which may be used to shape materials or monitor surface stresses. For instance, ribbons with an asymmetric triangular cross section take the shape of helices under the action of surface tension (Pham et al. 2013; **Figure 1c**).

Periodic grooves or ripple patterns on the surface of very soft gels are also altered significantly (Paretkar et al. 2014). The sharpest features are erased, or equivalently, high spatial Fourier frequencies are attenuated under the action of surface tension (**Figure 1d**). The relative change ΔA in the amplitude A of the grooves of wavelength λ is of order $\Delta A/A \sim \Upsilon/G\lambda \sim \ell_S/\lambda$. Moreover, the surface tension of these gels of polydimethylsiloxane may be modified by exposure to ultraviolet light, leading to some degree of control over the surface stress (Jagota et al. 2012).

Interfacial textures may finally emerge from the Biot instability, where creasing patterns result from compression along the surface of a soft solid. The threshold for creasing has recently been found to depend on the surface tension of the solid (Mora et al. 2011, Chen et al. 2012).

2.1.2. Rayleigh–Plateau instability. A paradigm of capillary-induced instability is the classical Rayleigh–Plateau instability: The liquid stream falling from a faucet breaks up into a collection of droplets with an overall lower surface-to-volume ratio (de Gennes et al. 2004). An analogous phenomenon occurs in the case of very soft solid cylinders.

Upon drying, a filament of acrylamide gel develops a tensed skin, which results in the growth of a peristaltic instability illustrated in **Figure 2a** (Matsuo & Tanaka 1992, Barrière et al. 1996).

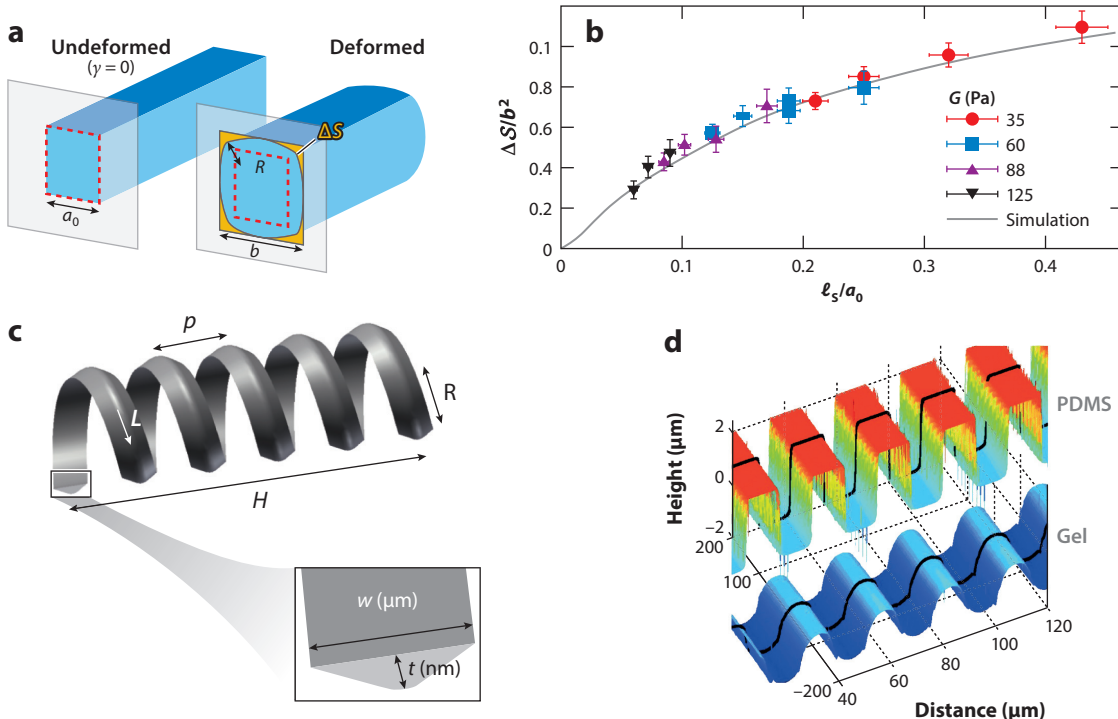


Figure 1

(a) Surface tension rounds off the corner of soft solids with a typical radius of curvature R of the order of ℓ_s . Adapted from Hui et al. (2002). (b) The initially square cross section of soft polyacrylamid gel is rounded off when immersed in silicone oil. Due to strong nonlinear effects, predicting the deformation is not trivial. However, the relative change of area $\Delta S/a_0$ follows a universal law when plotted against ℓ_s/a_0 . Adapted from Mora et al. (2013). (c) Ribbons with an asymmetric cross section deform under the action of solid surface tension. The edges with different sharpness are deformed unequally, leading to the curling of the ribbon into a helical shape (Pham et al. 2013). (d) The sharp texture of a soft solid's interface is smoothed when removed from its mold (Paretkar et al. 2014).

Even in the absence of a macroscopic skin, a strand of very soft agar gel released in toluene develops undulations along its axis (Mora et al. 2010). Axial modulations of the radius develop if the gel/toluene surface tension exceeds $\Gamma_c \sim G\rho_0$, where ρ_0 is the radius of the undeformed cylinder and G is the shear modulus of the gel (Figure 2). The instability develops preferentially large wavelengths. Related instabilities occur for fluid or solid cylinders embedded in another compliant matrix with various geometries, as has been studied theoretically and numerically (Henann & Bertoldi 2014, Taffetani & Ciarletta 2015, Xuan & Biggins 2016).

2.1.3. Modification of the apparent elastic properties of multiphase solids. Because interfaces couple to bulk mechanical properties of soft materials, we expect soft multiphase solids to display anomalous properties. According to the classical results from Eshelby (1957), an elastic matrix containing gas or liquid inclusions should appear softer than a plain material. Conversely, inclusions with a large shear modulus result in an overall stiffer material. Extending these results to include the effects of surface tension yields counterintuitive results. Indeed, deforming small inclusions tends to increase their area. Surface stresses thus oppose these deformations. As a consequence, a solid with soft inclusions may appear stiffer than a plain specimen. Ducloué et al. (2014) show that elastic porous materials do not follow Eshelby's prediction: Whereas air bubbles tend



Figure 2

(*a*) Upon drying, cylinders of acrylamide gels undergo a pearling instability. Adapted from Matsuo & Tanaka (1992). (*b*) When dipped in toluene, cylinders of soft agar gels develop a peristaltic instability driven by surface stresses. Adapted from Mora et al. (2010).

to weaken oil-in-water emulsions, the softening is less than expected. Style et al. (2015) even show experimentally that liquid droplets smaller than ℓ_S stiffen the material in which they are embedded. This effect has also been recently explored through molecular dynamics simulations (Liang et al. 2016).

As surface effects dominate at small scales, elastocapillary phenomena are expected to be relevant for the field of nanotechnologies, which has been expanding in the past decade. Understanding the mechanical properties of micro- and nanoscale devices is crucial for applications. Different studies conducted with metallic wires of submicrometer diameters reveal that their apparent stiffness deviates from predictions based on bulk values of the Young's modulus. For instance, apparent Young's moduli of silver or lead deduced from bending tests on nanowires depend on the geometry of the wires (Cuenot et al. 2004). For a wire of radius r and length L , surface effects indeed dominate bulk contributions in the bending stiffness when $r^3/L^2 < \ell_S$.

2.2. Wetting Soft Solids

In the previous configurations, surface stresses result from a single solid–fluid interface. However, many situations also involve contact lines where three different phases meet (e.g., a sessile droplet). In this section, we focus on the deformations at the vicinity of this singular contact line.

2.2.1. Neumann and Young's laws. Before describing the possible deformations induced by a liquid drop on a soft solid substrate, we recall the two classical laws of static wetting in the respective cases of liquid or rigid solid substrates, as sketched in **Figure 3** (de Gennes et al. 2004). Consider first a drop of liquid (phase 1) floating at the surface of a bath of immiscible liquid (phase 2) in another fluid (phase 3). At equilibrium, the vector balance of the tensions of the three interfaces applies at the contact line:

$$\Upsilon_{12}\mathbf{t}_{12} + \Upsilon_{13}\mathbf{t}_{13} + \Upsilon_{23}\mathbf{t}_{23} = \mathbf{0}, \quad 3.$$

where Υ_{ij} is the interfacial tension between phases i and j and \mathbf{t}_{ij} is the vector pointing along the $i-j$ interface (**Figure 3a**). Equation 3, known as the Neumann equation, sets the angles between the interfaces at the contact line.

The second classical result of wetting, the Young–Dupré equation, corresponds to the case of a liquid droplet deposited on a flat rigid substrate (**Figure 3b**). Balancing horizontal forces sets

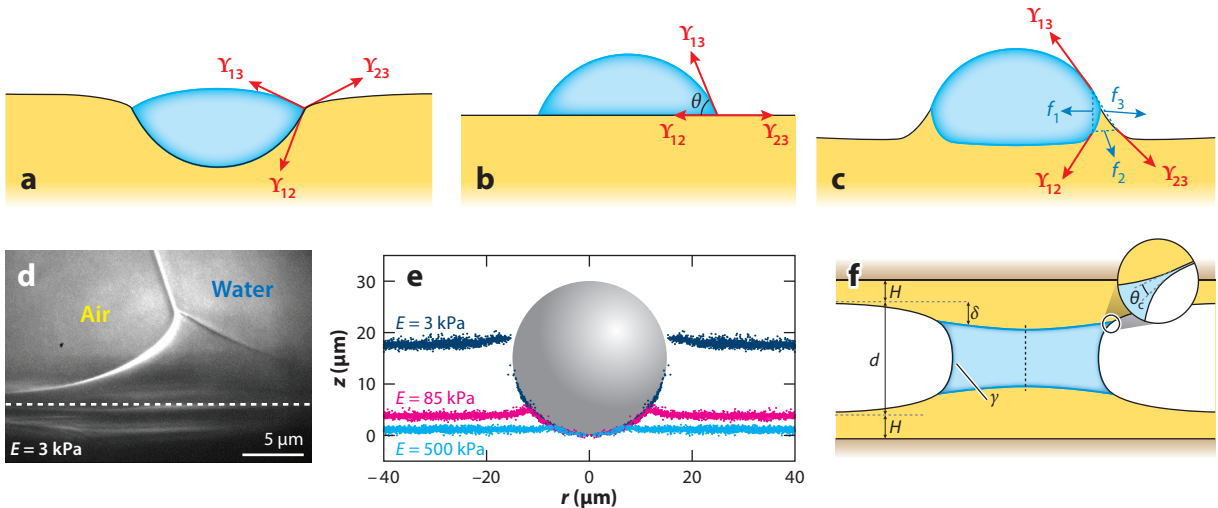


Figure 3

(a) Neumann balance of interfacial tensions at a contact line: The vector sum of surface tensions at the contact line vanishes. γ_{ij} is the surface stress associated with the $i-j$ interface. (b) Drop on a stiff solid. The contact angle is given by Young's law, which expresses the balance of horizontal projections of interfacial stresses. (c) On a soft solid, the upward component of the liquid surface tension is balanced by elastic stresses in the substrate, leading to the formation of a wetting ridge at the contact line. (d) Asymmetric wetting ridge induced by a water drop at the surface of a very soft silicone gel. Adapted from Park et al. (2014). (e) Profile of silicone gel layers deformed upon adhesion of silica particles of radius 15 μm. Adapted from Style et al. (2013c). (f) The shallow gap of thickness d separating two layers of thickness H may be squeezed by the negative Laplace pressure in a liquid bridge connecting both walls. Adapted from Wexler et al. (2014).

the value of the Young contact angle θ :

$$\gamma_{13} \cos \theta = \gamma_{23} - \gamma_{12}. \quad 4.$$

Although both Equations 3 and 4 have been successfully used to describe the wetting properties of liquids, these laws also constitute a subject of debate in the study of deformable solids. Early works by Lester (1961) and Rusanov (1978) question the validity of Young's law for the wetting of very soft materials. This question has recently been raised again as macroscopic values of ℓ_s can be obtained with very soft gels (Marchand et al. 2012; Weis et al. 2013, 2014; Style et al. 2017).

2.2.2. Static wetting and adhesion. Consider a liquid drop deposited on the initially horizontal surface of a soft material. If we neglect gravity, the drop takes the shape of a spherical cap and is characterized by its Young contact angle θ . However, Young's law seems to only provide an incomplete description of the situation, as it overlooks the vertical components of surface tensions. The liquid–gas surface tension indeed has a component normal to the solid surface that must be balanced. The wetting of a soft solid thus results in the formation of a ridge along the contact line of the drop (Figure 3c,d). Shanahan (1987) was a pioneer in describing theoretically the profile of the wetting ridge, and more recent studies are inspired by his early work (Jerison et al. 2011, Limat 2012). The shape and size of the ridge are set by a balance of surface stresses and elastic forces in the bulk of the soft solid so that the characteristic size of the deformed region is of the order of the elastocapillary length ℓ_s . The expected size of the ridge is very small for usual elastomers (submicrometric for $G \sim 1$ MPa), and the shape of wetting ridges has recently been measured experimentally in the context of wetting of soft gels (Pericet-Camara et al. 2008).

Jerison et al. (2011) report accurate measurements of the displacement field of wetting ridges in the vicinity of the contact line formed by a water drop deposited on an elastic substrate. Their theoretical model shows excellent agreement with experimentally measured displacement fields for the particular case of a drop contact angle $\theta = \pi/2$. One key ingredient is the introduction of the finite thickness of the layer of gel, which regularizes the divergence of the height of the ridge emerging in early models. In the general configuration, θ is not equal to $\pi/2$, and tangential displacements may also occur along the solid surface on which the drop rests (**Figure 3d**) (Das et al. 2011, Park et al. 2014).

Several authors discuss the validity of classical laws of wetting by Neumann and Young (Equations 3 and 4) in the wetting of soft solids (Das et al. 2011, Style & Dufresne 2012, Style et al. 2013a). Measuring the contact angles of drops of various sizes is one way to shed light on this problem. In particular, the contact angle of small drops on soft solids satisfies Neumann's criterion, whereas larger drops obey Young's law (Style et al. 2013a, 2017). The crossover between both regimes occurs for drops of radius $R \sim \ell_S$: At small scales, surface tension effects dominate over bulk forces. More generally, Neumann's balance of surface tensions applies in the close vicinity of a contact line, whereas Young's law applies at scales larger than ℓ_S .

The balance of surface tensions and bulk forces can be generalized to any combination of three phases, at least one of which is a soft solid. For instance, this is the case for the adhesion of stiff particles on soft substrates or soft particles on stiff substrates (see **Figure 3e**) (Salez et al. 2013, Style et al. 2013c, Andreotti et al. 2016) or for the shape of soft particles floating at the interface between two liquids (Mehrabian et al. 2016). In any configuration, deformations occur in the compliant phase on a scale ℓ_S around the triple line.

In a different geometry, a bridge of wetting liquid connecting two opposing soft walls also provides capillary adhesion due to its negative internal Laplace pressure. Consider two facing layers of soft material of thickness H deposited on stiff grounds and separated by a gap d (**Figure 3f**). If δ is the displacement of the surface of the soft layer, the induced strain scales as δ/H (we assume that the width of the liquid bridge is large in comparison with H). The corresponding stress $E\delta/H$ balances the Laplace pressure γ/d , leading to $\delta \sim (\gamma/E)(H/d)$. As a consequence, the gap of initial thickness d between these compliant walls may be squeezed if $d^2/H < \ell_S$ (Wexler et al. 2014).

2.2.3. Dynamical effects. The motion of a contact line at velocity V over a stiff substrate is usually described by the balance of viscous and interfacial stresses through the capillary number $Ca = \eta V/\gamma$, where η and γ are the viscosity and surface tension of the liquid, respectively (de Gennes et al. 2004). The deformation of elastic substrates by droplets strongly impacts the phenomena of dynamic wetting. Indeed, moving contact lines induce dissipation in the wetting ridges, which adds up to the usual viscous forces in the liquid. In early works, Shanahan (1988) experimentally and theoretically describes how viscous dissipation in the induced ridge may drastically slow down the spreading mechanism of a liquid drop. One signature of this effect is that the velocity of a drop sliding under gravity on a soft substrate is governed by the viscoelastic properties of the solid and may become independent of the liquid viscosity (Carré et al. 1996, Long et al. 1996). On soft solids, analogs of classical dynamic wetting laws involve a solid capillary number that compares surface tension to viscoelastic dissipation in the bulk of the substrate (Karpitschka et al. 2015).

A wetting ridge at a contact line constitutes a local and reversible roughness that enhances contact angle hysteresis on soft surfaces (Extrand & Kumagai 1996). As a result, rich contact line dynamics emerge on viscoelastic substrates: For instance, lines may move following a stick-slip motion in connection with the dynamics of the elastic ridge itself (Kajiyama et al. 2013, Karpitschka et al. 2015). Impact dynamics are also significantly affected by viscoelastic dissipation in the substrate.

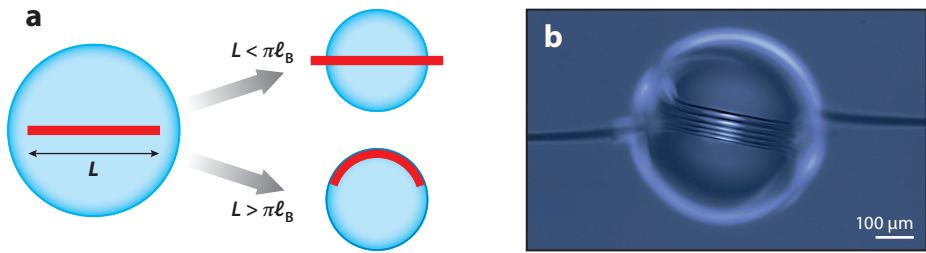


Figure 4

(*a*) A rod trapped in a droplet of a wetting liquid. Decreasing the volume of liquid eventually results in a compressive load on the rod by the surface tension of the deformed interface. If the length of the rod exceeds a critical capillary-bending length scale ℓ_B , the rod buckles. (*b*) The coiling of a rod inside a droplet (Schulman et al. 2017).

For instance, the retraction of a spread droplet after impact is significantly hindered (Alizadeh et al. 2013) and “it’s harder to splash on soft solids” (Howland et al. 2016).

The coupling of capillary forces to the deformations of elastic substrates may lead to interesting new applications. For instance, gradients in the elastic properties of the substrate may become the driving force for the motion of droplets along a soft substrate (Style et al. 2013b), a process termed durotaxis by analogy with cell motility. One may also hope for more efficient ways to harness transfer or dew collection, as the condensation processes on soft substrates have been shown to be more efficient than on stiff surfaces (Sokuler et al. 2010). Once the droplets are condensed on the soft substrates, they may even interact through a so-called Cheerios effect (Karpitschka et al. 2016).

3. CAPILLARY-INDUCED BENDING OF RODS

In the previous section, we described how a drop of water may deform a bulk material. Nevertheless, the elastocapillary length scale involved remains relatively small in usual situations. However, we know from our everyday experience that a macroscopic brush with unaligned bristles tends to form an elegant bundle when it is removed from a bath of water. In this section, we explore the bending deformation of slender structures by capillary forces as encountered in a wide variety of natural or engineered systems.

We first focus on the buckling of a single fiber by a liquid interface and derive a characteristic length scale based on the coupling between bending and capillary forces. The single fiber configuration is extended to the case of a brush or, more generally, to arrays of fibers. We then describe how van der Waals interactions replace capillary forces when the liquid evaporates and lead to stiction. We finally present other elastic modes of deformation involving stretching and twisting that are also relevant to microengineering applications.

3.1. A Rod in a Drop: Capillary Buckling

As a simple academic configuration, consider a thin rod trapped inside a droplet of wetting liquid in the absence of gravity or any other external field (Figure 4*a*). If the volume of liquid decreases (e.g., by evaporation), should we expect the confined rod to pierce the interface or, conversely, to match the spherical boundaries of its liquid container?

Piercing the interface would result in a compressive force $F = p\gamma \cos\theta$, where p is the perimeter of a cross section of the rod, γ is the liquid surface tension, and θ is the Young contact angle of the liquid on the rod (de Gennes et al. 2004). For the sake of simplicity, we assume that

the liquid perfectly wets the rod ($\theta = 0$). The general case with finite contact angle has also been addressed (Andreotti et al. 2011). Consequently, we expect the simply supported rod to buckle if F reaches the critical force derived by Euler, $F_c = \pi^2 EI/L^2$, where L is the length of the rod, I is the second moment of inertia, and E is the Young modulus of the material (Audoly & Pomeau 2010). In other words, the rod should buckle if its length exceeds the critical length, $L_c = \pi\ell_B$, where the capillary-bending length ℓ_B is given by Cohen & Mahadevan (2003):

$$\ell_B = \sqrt{\frac{EI}{p\gamma}}. \quad 5.$$

Capillary-bending length:

$\ell_B = \sqrt{Er^3/8\gamma}$ for a cylinder,

$\ell_B = \sqrt{\frac{Et^3}{24(1-\nu^2)\gamma}}$ for a lamella

In the case of a cylindrical rod of radius r , we obtain $p = 2\pi r$, $I = (\pi/4)Er^4$, and $\ell_B = \sqrt{Er^3/8\gamma}$. Thin lamellae of width w and thickness t with $t \ll w$ are also common in academic studies as well as in practical situations (Neukirch et al. 2007). In this geometry, we similarly obtain $p = 2w$ and $I = Et^3w/12(1 - \nu^2)$, where ν is the Poisson coefficient of the material, which leads to $\ell_B = \sqrt{Et^3/24(1 - \nu^2)\gamma}$.

This capillary-induced buckling mechanism has, for instance, been proposed to explain the formation of rings of carbon nanotubes inside cavitation bubbles (Martel et al. 1999). If the length of the flexible rod is large compared to the perimeter of the droplet, the rod may eventually form a coil into the droplet, as illustrated in **Figure 4b** (Roman & Bico 2010, Schulman et al. 2017). In a different field, capillary-induced coiling is also crucial for the capture of prey by some orb-weaver spiders. Although drag lines spun by spiders are renowned for their amazing mechanical properties, capture threads also display unique damping properties that prevent impacting prey from bouncing off the web (Vollrath & Edmonds 1989). The damping mechanism was only recently demonstrated (Eletto et al. 2016). The spiraling thread spun by the spider is actually significantly longer than its apparent length. The excess length is stored in coils formed into minute droplets deposited along the thread by the spider. In contrast with an elastic string, where the pulling force increases linearly with strain, the force required to extend the thread is almost constant (equal to F_c if viscous forces are neglected). After being stretched, the coil reforms slowly due to the high viscosity of the droplets, which ensures the efficient damping of impacting prey.

3.2. Elastocapillary Rackets: Measuring the Capillary-Bending Length Scale

How can ℓ_B be measured? Determining the critical buckling length accurately would not be convenient. However, measuring the deflection induced by a lateral load could be more efficient.

3.2.1. Scaling law. A simple technique consists of bending a ribbon into the shape of a racket and assembling both ends with some wetting liquid (**Figure 5a**). At equilibrium, both extremities meet at a precise contact point. The shape of the lamella follows Euler elastica mechanics (Audoly & Pomeau 2010) and is universal for such boundary conditions. However, the bending elastic energy stored in the lamella depends on its size:

$$U_b \sim \frac{EI}{L^2} L, \quad 6.$$

where the length L of the bent part of the ribbon also gives the scale for its curvature. Increasing the size of the racket reduces the elastic energy but also costs surface energy. In the case of flexible lamellae of width w , the surface energy of the system is proportional to

$$U_s \sim \gamma w(L - L_t), \quad 7.$$

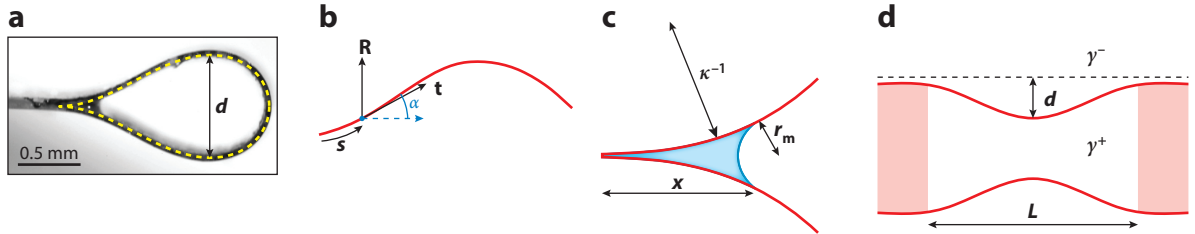


Figure 5

(a) An elastocapillary racket. The opposite strands of a strip looped on itself are maintained by a liquid meniscus. The shape of the loop is compared with a numerical solution of the Euler elastica equation (Py et al. 2007b). The width d of the racket provides a measure of ℓ_B . (b) The coordinates used in the elastica equation. (c) A close-up of the capillary bridge in the vicinity of the strands' contact point. (d) A floating flexible frame deflected by a contrast in surface tension. The surface pressure, $\Pi = \gamma^+ - \gamma^-$, can be inferred from monitoring the amplitude of deflection d .

where L_t is the total length of the lamella. Minimizing the global energy of the system thus sets the size of the racket (Cohen & Mahadevan 2003, Py et al. 2007a):

$$L \sim \ell_B. \quad 8.$$

A simple way of assessing ℓ_B thus consists of measuring the width d of the racket. The numerical prefactor has to be determined numerically: $d = 1.26 \ell_B$. The same scaling can be generalized to rods, although the derivation of the capillary energy slightly depends on the volume of liquid in the meniscus connecting the facing extremities (Py et al. 2007a).

3.2.2. Boundary conditions. The Euler elastica equation has to be solved in order to predict the exact shape of the racket (Audoly & Pomeau 2010). For a beam of bending stiffness EI , the evolution of the angle α between the tangent t to the lamella and the horizontal is determined by a moment balance along a portion ds of the beam:

$$EI \frac{d^2\alpha}{ds^2} \mathbf{e}_z + \mathbf{t} \times \mathbf{R} = 0, \quad 9.$$

where \mathbf{R} is the constant vectorial tension acting on the beam, \mathbf{e}_z is the direction perpendicular to the plane, and s is the curvilinear coordinate (Figure 5b). This equation can be solved through standard shooting methods for given boundary conditions at both extremities. Although the position and the slope of the tips are trivial, the balance between capillary forces and bending stiffness results in a specific boundary condition at the contact point of the merged extremities: The initial curvature $\kappa = d\alpha/ds$ is proportional to $1/\ell_B$.

The precise derivation of the curvature jump at the contact point requires variational methods (Majidi & Adams 2009). However, this initial curvature can be viewed as a simple moment balance (Figure 5c). If we take x to be the lateral extension of the liquid meniscus at the junction between both strands of the racket, its radius of curvature r_m is proportional to κx^2 (we assume $x \ll \kappa^{-1}$). The resulting Laplace pressure is thus of the order of $P \sim \gamma/r_m$, which leads to a force $F \sim Pxw$, where w is the width of the beam. The corresponding moment $Fx \sim \gamma w/\kappa$ balances the bending moment EIk , which finally leads to

$$\kappa^{-1} \sim \ell_B. \quad 10.$$

The numerical prefactor depends on the exact configuration. In the case of a pair of merging lamellae, we find $\kappa^{-1} = \ell_B/\sqrt{2}$ (Roman & Bico 2010). The induced curvature is independent of the quantity of liquid and can even be applied to dry adhesion (Majidi & Adams 2009).

3.2.3. Capillary-induced deflection of flexible frames. A contrast in surface tension between each side of a flexible frame floating at the surface of water can also induce a deflection of the frame. Measuring the amplitude of this deflection constitutes an elegant way to assess surface pressures on a Langmuir trough (Hu et al. 2003, Zell et al. 2010).

Consider a rectangular frame of length L with two rigid sides floating at the surface of water. Adding surfactant molecules outside the frame results in a contrast in surface tension $\Delta\gamma$, which induces a deflection of the edges of the frame of amplitude d (**Figure 5d**). The corresponding elastic energy scales as $EIL(d/L)^2$, whereas the gain in surface energy is proportional to $\Delta\gamma dL$. As a result, the amplitude varies linearly with the surface pressure:

$$d \sim \frac{L^2}{EI} \Delta\gamma. \quad 11.$$

The same concept has recently been used to estimate the local surface tension of a soap film (Adami & Caps 2015).

As a conclusion of this section, the capillary-bending length prescribes the characteristic curvature surface tension may induce on a slender structure. An alternative way to define this length scale would be to deposit the slender structure on a cylinder of radius R coated with a wetting liquid. The structure spontaneously wraps the cylinder for $R > \ell_B$. In the opposite situation, the structure remains undeformed.

So far, we have focused on a single rod. In the next section, we describe the bundling of arrays of filaments induced by capillary forces.

3.3. Elastocapillary Self-Assembly

In the previous section, we described how an isolated slender structure is prone to buckle under the action of surface tension if its length exceeds the capillary-bending length ℓ_B . However, many practical situations involve arrays of structures (**Figure 6**). For instance, the possible collapse of microstructures is an important constraint in the design of microelectromechanical systems (MEMS). Indeed, standard lithography processes involve the evaporation of a solvent, which generates liquid bridges that can be fatal for minute microstructures (Abe & Reed 1996, Tas et al. 1996, Maboudian 1997). In materials science, many works on carbon nanotube forests have reported the formation of pyramidal bundles (Lau et al. 2003) or cellular patterns (Chakrapani et al. 2004, Correa-Duarte et al. 2004) after the evaporation of a solvent. Similar structures are also commonly observed with arrays of micropillars obtained with soft polymers (Duan & Berggren 2010, Hu et al. 2015, Kim et al. 2016). Intriguing twisted bundles may even be observed (Pokroy et al. 2009, Kang et al. 2010). In materials science, beautiful works have recently been devoted to elastocapillary engineering of filamentary materials (Tawfick et al. 2016). For instance, elegant nanotube gardens are produced by combining the controlled growth of carbon nanotubes on silicon substrates and capillary bundling (García et al. 2007; De Volder et al. 2010, 2011). Harnessing capillary forces to build complex structures paves the way for interesting applications such as field emission (Wang et al. 2016), enhanced molecule detection (Hu et al. 2010), or surfaces with tunable color (Chandra & Yang 2010).

Finally, such capillary-induced bundling is not limited to engineered systems but is also frequent in nature. For instance, the barbules of bird feathers may form fatal clumps when contaminated by oil (Duprat et al. 2012). At a smaller scale, the adhesive setae from some insect species may also form bundles (Gernay et al. 2016).

3.3.1. Bundles: from engineered systems to model experiments. What are the physical ingredients driving elastocapillary bundling? Model experiments conducted with macroscopic brushes show that bundling involves a cascade of pairing reminiscent of coalescence mechanisms (Bico et al.

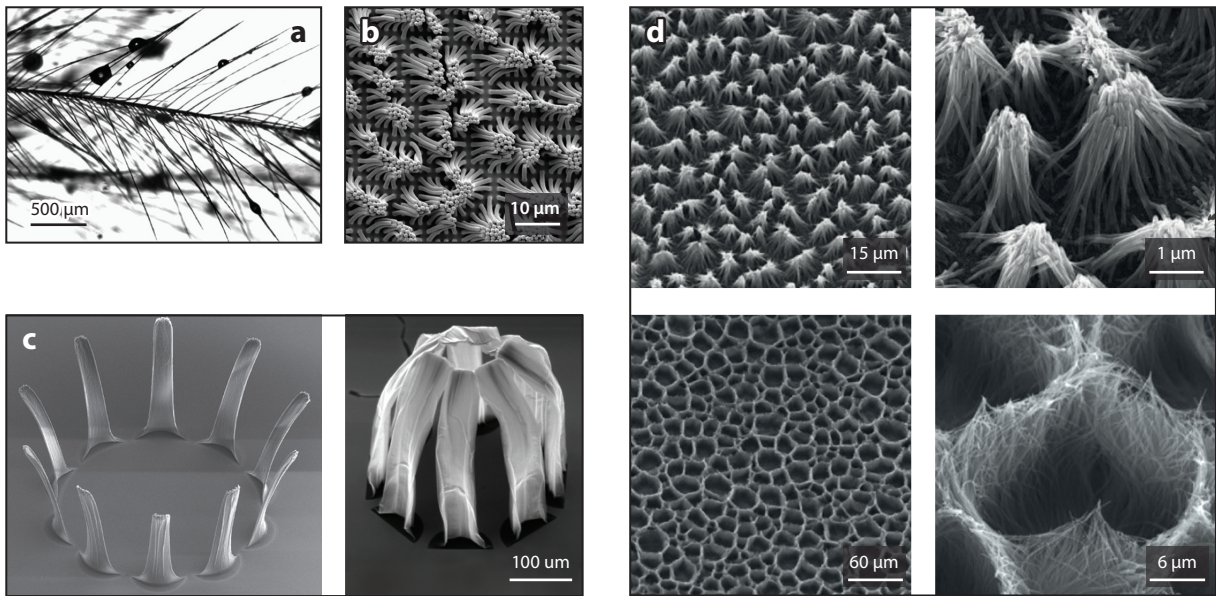


Figure 6

Examples of capillary-induced bending and eventual bundling of an array of slender structures. (a) Oil-contaminated barbules of a feather (Duprat et al. 2012). (b) An array of bundled soft polymeric pillars (Chandra & Yang 2009). Self-assembled arrays of carbon nanotubes into (c) nanogardens (De Volder et al. 2010) or (d) pyramidal bundles or cellular patterns (Correa-Duarte et al. 2004).

2004, Kim & Mahadevan 2006, Py et al. 2007a): As the brush is withdrawn from a bath of wetting liquid, pairs of smaller bundles merge into large bundles that in turn merge into even larger bundles (**Figure 7a**). However, an alternative mechanism involving simultaneous bundling is also relevant during the drying of arrays of dense pillars. In the following sections, we present both mechanisms.

3.3.2. Merging a pair of beams. As an elementary model configuration, consider two parallel plates separated by a distance d that is small in comparison with the capillary length ℓ_c . If the lamellae were rigid, Jurin's law would dictate that the equilibrium height of rise is $b_J = 2\gamma/\rho gd$ (de Gennes et al. 2004). However, the low pressure in the rising liquid tends to bring both lamellae together, which results in a thinner gap and a higher equilibrium height. The rising process eventually stops when the cost in elastic energy corresponding to the bending of the lamellae compensates the gain in surface energy. If the lamellae are long enough, the liquid reaches an equilibrium height at a fixed distance L_{stick} from the clamping base of the lamellae (**Figure 7b**). This distance is readily derived with the same energy argument used in the previous section to describe the size of a racket.

In the limit $L_{\text{stick}} \gg d$, the typical curvature of the bent lamella d/L_{stick}^2 results in the elastic energy:

$$\mathcal{U}_b \sim EI \left(\frac{d}{L_{\text{stick}}^2} \right)^2 L_{\text{stick}}. \quad 12.$$

As in the case of the racket, the surface energy reads

$$\mathcal{U}_s \sim \gamma w(L_{\text{stick}} - L_t), \quad 13.$$

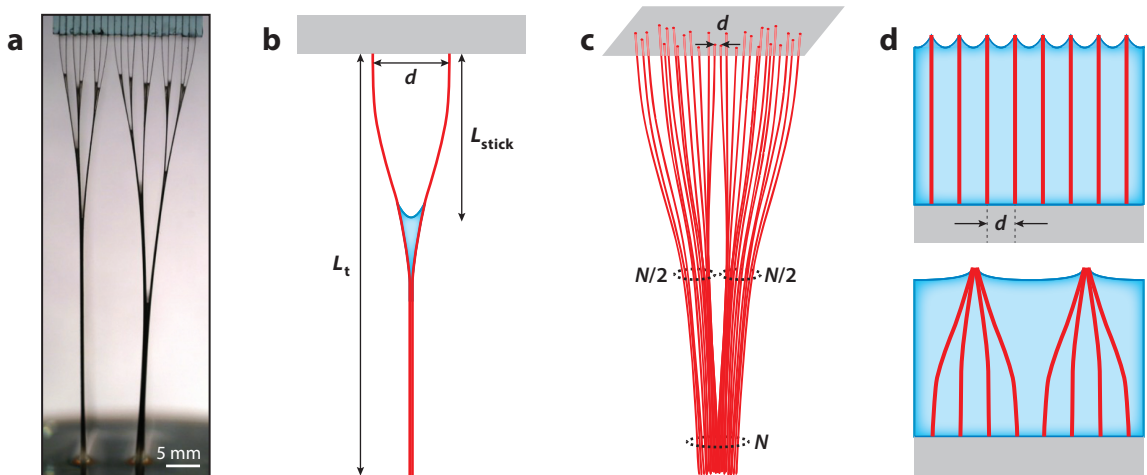


Figure 7

(a) Bundling mechanism involving a cascade of pairing as a brush of long fibers is withdrawn from a bath of wetting liquid (Bico et al. 2004). (b) Pair of parallel beams of total length L_t and separated by a spacing d adhere up to a distance L_{stick} from their clamping base when put in contact with a wetting liquid. (c) Bundling sequence of a two-dimensional array of fibers: two bundles of average size $N/2$ merge into a large bundle of size N . (d) Alternative mechanism involving a single step as an initially immersed array of fibers is progressively dried. Adapted from Tawfick et al. (2016).

for lamellae of total length L_t and width w . Minimizing the global energy $\mathcal{U}_b + \mathcal{U}_s$ with respect to L_{stick} provides the sticking length:

$$L_{\text{stick}} \sim \ell_B^{1/2} d^{1/2}, \quad 14.$$

as validated experimentally for both arrays of lamellae (Bico et al. 2004, Kim & Mahadevan 2006) and of cylindrical rods (Py et al. 2007a).

3.3.3. Dynamics. In terms of dynamics, different timescales can be defined as a function of the stiffness of the lamellae. In the case of rigid lamellae, the interplay between the viscous flow driven by surface tension and the limiting hydrostatic pressure leads to a typical rising time (de Gennes et al. 2004):

$$\tau_r \sim \frac{\eta \gamma}{(\rho g)^2 d^3} \sim \frac{\eta \ell_c^2}{\gamma d^3}. \quad 15.$$

In the opposite case of long, flexible lamellae, the dynamics are dominated by the closure of the gap induced by the low pressure in the rising liquid. In this situation, the resulting viscoelastic timescale is given by Duprat et al. (2011):

$$\tau_{ve} \sim \frac{\eta}{\gamma} \frac{L_t^6}{d^3 \ell_B^2}. \quad 16.$$

Nevertheless, this relation is not universal and we expect the elastocapillary rise between circular rods to follow different timescales. The rising liquid can indeed flow along the curved corners formed along contacting rods.

Another timescale has also been proposed to describe a configuration where the liquid flows from the clamp to the tip (Aristoff et al. 2011, Taroni & Vella 2012): $\tau_b \sim \eta \ell_B / \gamma$. A future

comprehensive study of elastocapillary dynamics involved in the different practical situations would be highly valuable.

3.3.4. Elastocapillary coalescence. The pairing mechanism presented in the previous section can be adapted to larger scales. A bundle composed of N beams indeed results from the grouping of two smaller bundles of average size $N/2$. Both smaller bundles may be considered as effective beams with a stiffness multiplied by $N/2$ (assuming that the presence of a thin layer of fluid lubricates the relative sliding of the beams) and a separating distance that is also amplified (**Figure 7**). The effective distance is simply $Nd/2$ for a simple linear array and proportional to $N^{1/2}d$ in the case of a 2D lattice. Putting this effective stiffness and distance in Equation 14, we obtain the merging length for a bundle of size N for a linear array: $L_{\text{stick}}(N) \sim N^{3/4}\ell_B^{1/2}d^{1/2}$. In the case of a 2D lattice, the scaling is slightly different: $L_{\text{stick}}(N) \sim N^{3/8}\ell_B^{1/2}d^{1/2}$. The inversion of this relation prescribes the maximum size N_{\max} of a 2D bundle composed of flexible elements of length L_t :

$$N_{\max} \sim \frac{L_t^{8/3}}{\ell_B^{4/3}d^{4/3}}, \quad 17.$$

in agreement with experimental data obtained with model brushes (Py et al. 2007a).

3.3.5. Simultaneous bundling. Although the previous model is relevant for long brushes withdrawn from a liquid bath, alternative scenarios have been developed to describe the drying of 2D arrays of dense pillars initially immersed in a volatile liquid. In this approach, bundles are formed in a single step when the interface of the liquid reaches the top of the pillars (**Figure 7d**). For pillars of radius r , deforming the interface corresponds to a cost in surface energy of the order of γr^2 per pillar. As a consequence, pillars mutually attract through lateral capillary forces (Kralchevsky & Nagayama 2000, Chandra & Yang 2009). However, forming a bundle also results in bending elastic energy. For a bundle containing N pillars, the average deflection is proportional to $N^{1/2}d$. Consequently, the elastic energy per bent pillar scales as Er^4Nd^2/L^3 . Comparing surface and bending energies, we obtain the scaling $N_{\max} \sim (L/L_s)^3$ for the maximum size of a bundle, where $L_s = (Er^2d^2/\gamma)^{1/3}$. This scenario is consistent with experimental data obtained with silicon nanorods (Zhao & Fan 2006) or epoxy micropillars (Chandra & Yang 2010) corresponding to pillar densities $r/d \sim 0.2$.

3.3.6. Size distribution. Although both bundling mechanisms provide a maximum size N_{\max} for the self-assembled clusters, wide size distributions are observed in experiments (Boudaoud et al. 2007). The shapes of these distributions rely on dynamics. For instance, in the cascade mechanism, the first step consists of forming pairs. However, about one-third of the flexible structures remain statistically unpaired, as their first neighbors are already paired. Successive associations can later on lead to bundles of size three, four, five, and, finally, to any size below N_{\max} . The distributions can be rescaled by N_{\max} , and different approaches have been proposed to describe this distribution from crude mean field (Boudaoud et al. 2007) to more sophisticated dynamical models, such as arrays of rigid plates with elastic hinges (Bernardino & Dietrich 2012, Wei & Mahadevan 2014) or idealized brushes of parallel lamellae (Singh et al. 2014, Hadjitoftis et al. 2016). The comparison of the two last references with experimental data is particularly convincing. Nevertheless, a comprehensive study of the size distribution in the case of 2D arrays of pillars still remains to be conducted both experimentally and theoretically.

Combining buckling and bundling mechanisms may also explain qualitatively different morphologies observed experimentally, such as pyramidal bundles or cellular patterns. Indeed, isolated pillars or small bundles may buckle and collapse on the substrate, whereas wider bundles may resist

and form the walls of the observed cells (Chioldi et al. 2010, Tawfick et al. 2016). However, further work would be necessary to quantitatively confirm such a scenario. The field of computer graphics has recently been expanding, and very impressive simulations combine interfacial hydrodynamics with the deflection of thousands of flexible fibers (Fei et al. 2017). Such powerful tools will certainly bring new insights into bundling mechanisms.

3.3.7. Stiction. Although capillary forces can induce the formation of bundles, we might expect elastic microstructures to recover their initial shape once the liquid has totally evaporated. However, collapsed structures generally remain permanently deformed due to attractive molecular forces, which is a major issue for MEMS (Abe & Reed 1996, Tas et al. 1996, Maboudian 1997) or microcontact printing (Hui et al. 2002, Sharp et al. 2004). Van der Waals surface energy W_a involved in contact adhesion is indeed of the same order of magnitude as the surface tension. In the case of contact between flat surfaces, the relations between elasticity and surface tension can be adapted by simply replacing γ by W_a (DelRio et al. 2005). When cylindrical rods are involved, the actual contact width a depends on a balance between adhesion energy and material stiffness, $a \sim (W_a r^2/E)^{1/3}$ (Chaudhury et al. 1996). Consequently, γ should be replaced by $W_a^{4/3}/(Er)^{1/3}$ (Roca-Cusachs et al. 2005, Kim et al. 2016).

3.4. Collapsing Tubes and Channels

The previous sections show how capillary forces may induce the collapse of simple slender structures such as rods or lamellae. However, similar effects are also observed in tubular geometries. For instance, tongues of hummingbirds have a peculiar gutter shape that spontaneously closes by capillarity when in contact with a liquid. Nectar is then safely transported through the self-assembled straw (Rico-Guevara & Rubega 2011).

However, the deformation of compliant channels induced by capillary forces may be tragic in other situations. The collapse of lung airways of premature babies is a major issue that has motivated numerous academic studies (Groberg & Jensen 2004). If a flexible tube internally lined with a liquid collapses, the capillary energy reduces with the liquid vapor surface (**Figure 8a**). The mechanism involves a snap-through instability that occurs when surface tension forces overcome the rigidity of the tube's cross section (Hazel & Heil 2003, Ducloué et al. 2017). As a crude

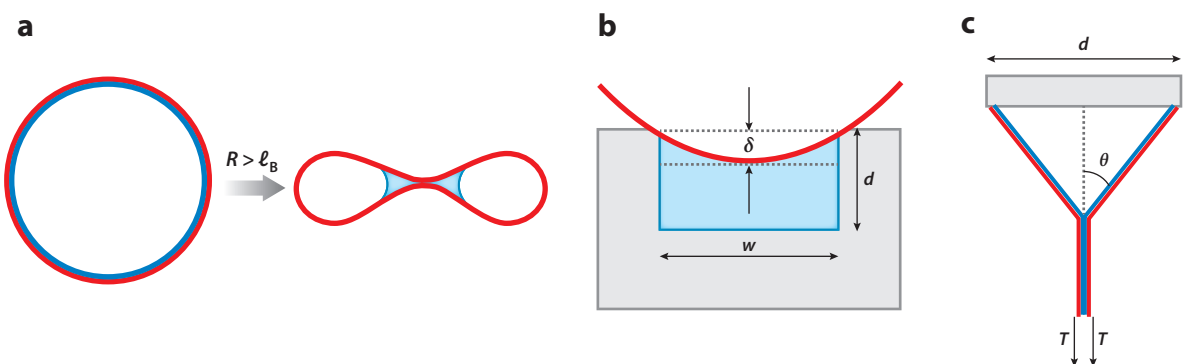


Figure 8

(a) Possible collapse of a flexible tube of radius $R > \ell_B$ lined with a layer of liquid. (b) Deflection of a channel covered with a flexible lid. (c) Adhesion of a pair of lamellae subjected to a tensile load T in the ideal case where the lamellae do not have any bending rigidity but are unstretchable.

approximation, the problem is similar to the deformation of flexible frames presented in Section 3.2.3. A tube of radius R and wall thickness t is expected to buckle and eventually collapse for $R \gg \ell_B \sim \sqrt{Et^3/\gamma}$ (note that the relevant rigidity is based on the deformation of the cross section and not on the bending of the tube along its length, as in bundling).

From an engineering perspective, soft microfluidic channels may also deform under a strong Laplace pressure drop, which may enhance the flow velocity (Anoop & Sen 2015) or capillary rise (Cambau et al. 2011). In an ideal situation, a microfluidic channel may be viewed as a rigid groove of width w and depth d covered with a plate of thickness t (**Figure 8b**). The deflection δ induced by a pressure drop of order γ/d is readily estimated from a torque balance. The capillary moment per unit length scales as $\gamma w^2/d$, and the restoring moment from the bent plate corresponding to a typical curvature δ/w^2 is proportional to $Et^3\delta/w^2$. At equilibrium, the induced deflection should thus follow

$$\delta \sim \frac{w^4}{d\ell_B^2}. \quad 18.$$

The closing condition is thus similar to the adhesion of wet lamellae, $w \sim \ell_b^{1/2} d^{1/2}$, in agreement with experiments conducted with a model setup (Cambau et al. 2011). However, the actual problem is more complex, as it usually also involves stretching of the channel wall.

3.5. Capillarity Against Tension

Deformations induced by capillary forces are not limited to bending modes. For instance, Duprat & Protiere (2015) and Legrain et al. (2016) recently investigated the capillary adhesion of a pair of parallel rods or ribbons subjected to a tensile force.

As a model experiment, consider a pair of vertical lamellae of length L clamped at their upper extremities with a separating distance d such that each is subjected to a constant tension T per unit width (e.g., by hanging weights). We assume that the lamellae do not have any bending rigidity but are unstretchable. Upon introduction of some wetting liquid inside the spacing, the lower parts of the lamellae join at a distance L_{stick} from the clamp and form an angle θ with the vertical, as sketched in **Figure 8c** ($\tan \theta = d/2L_{\text{stick}}$). The interfacial energy (per unit width) gained by a lamella by adhering to its neighbor is $\mathcal{U}_\gamma = \gamma(L - L_{\text{stick}}/\cos \theta)$. As a result of sticking, the bottom point of the lamella lifts by an amount $\delta = d(1 - \cos \theta)/2 \sin \theta$, inducing a work $W_T = -T \delta$ of the tension force. The equilibrium Y shape formed by the adhered lamellae is found by maximizing $W_T + \mathcal{U}_\gamma$ with respect to θ , yielding

$$\cos \theta = \frac{T}{T + \gamma}, \quad 19.$$

which is reminiscent of the equation defining the Young contact angle. Note that the tension is not necessarily constant and may depend on θ . For instance, merging lamellae of length L and thickness t clamped at both ends without any prestrain induce a progressively increasing tension. Indeed, the corresponding strain can be estimated from elementary geometry as $\varepsilon = \frac{1-\cos \theta}{\sin \theta} \frac{d}{L}$, which leads to the tension $T = Et \frac{1-\cos \theta}{\sin \theta} \frac{d}{L}$. In such a case, the adhesion angle θ is determined by solving the nonlinear equation obtained by putting the value of $T(\theta)$ in the expression for $\cos \theta$.

4. DROPS AND ELASTIC SHEETS

In the previous section, we have described how capillary forces may buckle or, more generally, deflect a rod. Can these results be extended to plates? Bending a plate of thickness b along a single

direction involves the same bending elastic energy proportional to b^3 , as in the case of a rod. However, we know that wrapping an orange with a sheet usually leads to complex folds and wrinkles. Indeed, simultaneously bending a sheet in two different directions also involves stretching (Audoly & Pomeau 2010). Because stretching energy scales linearly with b , the cost of stretching is very high compared to bending in the limit of small thicknesses. Consequently, a thin sheet complies whenever possible with geometrical constraints or mechanical load by pure bending, preserving the distances along its surface, with important consequences for elastocapillary phenomena.

In this section, we first present the conditions for the spontaneous wrapping of a liquid droplet within a sheet. We then focus on the capillary adhesion of a thin sheet on a rigid substrate as an illustration of how geometrical constraints may impose a finite stretching of the sheet. Finally, we describe the case of a small droplet deposited on a floating sheet and show how the stretching modulus of the plate becomes a relevant parameter due to the tension induced by capillary forces.

4.1. Capillary Origami

Although complex 2D structures are commonly obtained through conventional lithography, building 3D micro-objects remains challenging. Capillary forces constitute a promising tool to self-assemble micro-objects in two and even in three dimensions (Boncheva & Whitesides 2005, Mastrangeli et al. 2009). What are the conditions needed to build capillary origami structures?

4.1.1. Folding hinges. Impressive 3D structures have been obtained by depositing a tiny droplet of water on flat templates with designed hinges (Legrain et al. 2014). When the droplet comes into contact with the template, capillary forces acting at the contact line tend to pull the flaps, and the positive Laplace pressure tends to push the hinge away (**Figure 9a**). The global effect is a moment of the order of γL per unit width, where L is the length of the flaps (here we assume that the radius of the droplet is comparable to the size of the structure). Consequently, the hinge closes with angle $\alpha \sim \gamma L/C$, where C is the rotational stiffness of the hinge per unit width. Surface

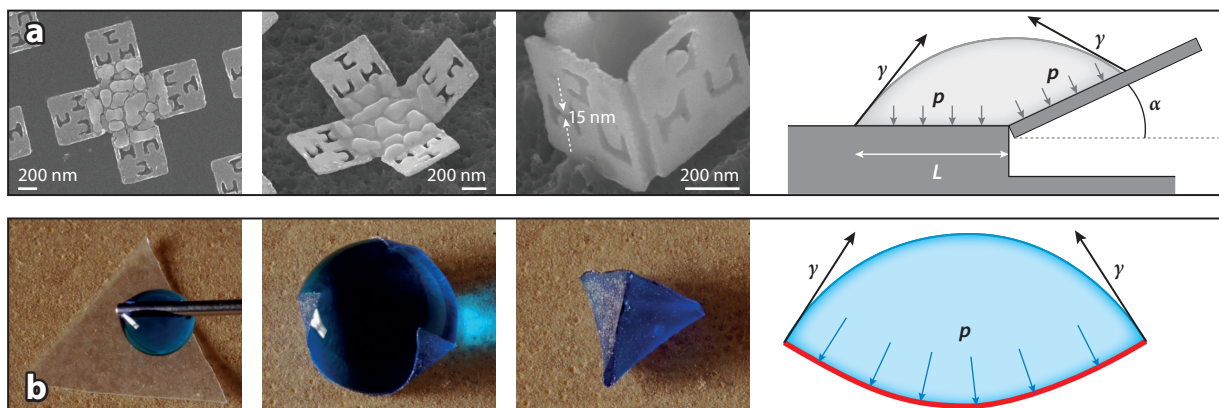


Figure 9

Folding elastic plates with surface tension. (a) Capillary forces resulting from melting a thin layer of tin induce a moment and, consequently, a rotation along the hinges at a submicrometer scale. Reprinted from Cho et al. (2009). (b) A droplet deposited on a thin elastic sheet may bend the sheet to minimize the liquid–air interface, leading to the spontaneous wrapping of the droplet (Py et al. 2007b).

tension forces may even be activated on demand using a small quantity of tin deposited on the hinges (Syms et al. 2003, Filipiak et al. 2009). As temperature increases, the tin melts into a liquid droplet whose surface tension may fold the hinge (**Figure 9a**). Elegant submicrometer self-folding cases have been produced with such techniques (Cho et al. 2009).

4.1.2. Folding elastic plates. In a technologically simpler situation, a featureless plate (without hinges) may also fold with a very good reproducibility but now involves distributed elastic bending of the plate. When a droplet of liquid is deposited on a flexible template (Py et al. 2007b), the torque induced by capillary forces tends to bend the plate into a shape that depends on the volume of liquid. The radius of the droplet is here comparable to the size of the template so that the contact line remains pinned at the edges of the plate (the liquid partially wets the plate). Experimentally, as the liquid evaporates, the structure may fold on itself (see **Figure 9b**) or, conversely, open again if the bending rigidity is too large. Although computing in detail the nonlinear coupling between the deformable droplet and the folding plate is complex (Brubaker & Lega 2016b), theoretical models with simplified (Chen et al. 2010, de Langre et al. 2010) or bidimensional (Péraud & Lauga 2014, Brubaker & Lega 2016b) geometries describe almost quantitatively the evolution of the structure as a function of the volume of the droplet. In terms of scaling, the closing condition for a plate of size L is simply set by a balance of the capillary torque with the elastic response EI/L of the plate as a curvature of order $1/L$ develops. The structure is thus expected to close for $L > L_c$ with

$$L_c \sim \ell_B.$$

The numerical prefactor depends on the actual shape of the template (Py et al. 2007b). Additional effects such as contact line depinning (Péraud & Lauga 2014, Brubaker & Lega 2016b) or gravity can also be taken into account and lead to a large number of competing stable equilibrium states. The equilibrium configurations observed in practice depend on the mode of preparation of the system. An interesting example is when a drop impacts the elastic sheet, triggering capillary folding. Different fold states are observed as a function of the impact velocity (Antkowiak et al. 2011). We believe that the dynamics of elastocapillary systems, a challenging problem due to nonlinear interactions, could become an interesting general subject for future work.

From a more academic point of view, many studies have been dedicated to the case of a partially wetting droplet deposited on a long, flexible strip (Antkowiak et al. 2011, Rivetti & Neukirch 2012), which can be approximated as a 2D problem. In this case, the capillary moment is limited by the size of the droplet and scales as $\gamma R w$, where w is the width of the strip. If the strip deflects with an angle α , the resulting curvature induced to the strip is of the order of α/R , and the elastic restoring moment scales as $EI\alpha/R$. At equilibrium, the deflection angle thus reads

$$\alpha \sim (R/\ell_B)^2.$$

Depending on the boundary conditions and initial conditions, the strip may simply bend, as in the case of a droplet sitting on the cantilever of an atomic force microscope (Bonaccurso & Butt 2005), but also undergo snap-through instabilities (Fargette et al. 2014) on prebuckled strips. Finally, if the elastic stiffness varies along the strip, the drop should shift from stiff to soft regions, as it is energetically favorable to minimize the area of the drop in contact with air. This effect would then constitute an analog for the durotaxis phenomenon observed with bulk materials (Style et al. 2013b).

The more general case of a sessile drop sitting on a flexible disc was considered by several authors in the limit of linear plate theory, which fails as soon as the deflections become comparable to the thickness of the plate (Kern & Müller 1992, Olives 1993, Brubaker & Lega 2016a). In fact, the corresponding axisymmetric bending solutions also involve compressive azimuthal stresses, which lead to buckling and symmetry breaking.

4.1.3. Applications and practical situations. Capillary wrapping is a robust feature that is observed on various systems with different wettability (Geraldi et al. 2013, Bae et al. 2015). At nanoscales, computer simulations even show that graphene sheets are expected to wrap around nanodroplets (Patra et al. 2009). Several practical applications of capillary origami have been envisioned.

For instance, 3D photovoltaic cells obtained by capillary origami could exhibit enhanced yield (Guo et al. 2009), and self-folding microcontainers could be used to encapsulate drugs (Fernandes & Gracias 2012). Elastic self-closing structures are also present in nature: The flowers of some species of water lilies are able to close and trap an air bubble when immersed. This phenomenon has recently inspired the development of elastopipettes, which can capture a given volume of liquid from a bath and release it to another one (Reis et al. 2010, Meng et al. 2014).

Once the structure is closed, an additional electric field applied between the droplet and a substrate covered with a dielectric layer may be used to reopen the structure: The charged droplet entrapped in the folded structure is attracted by the ground, and the structure tends to unfold as the voltage increases (Piñeirua et al. 2010). Similar to classical electrowetting, a characteristic voltage, $U_c = \sqrt{\gamma d / \epsilon}$, can be defined, where d is the thickness of the dielectric layer and ϵ is its permittivity. This type of actuation was proposed as a way to produce iridophores mimicking the color change of particular cells on the skin of cephalopods (Manakasettharn et al. 2011). Finally, magnetic actuation has been proposed as a way to manipulate ferrofluid droplets wrapped in a thin plate (Jamin et al. 2011).

4.1.4. Geometrical limit in capillary origami ($R \gg \ell_B$). In most practical examples presented above, the size of the thin plate is close to the folding threshold, $R \sim \ell_B$, so that capillary and elastic forces are of comparable magnitude. Another interesting limit corresponds to the case where capillary forces strongly dominate over bending, $R \gg \ell_B$, but are still unable to induce significant stretching. Paulsen et al. (2015) conducted beautiful experiments with polystyrene sheets of thickness $t \sim 100$ nm corresponding to $R/\ell_B > 10^2$, producing strongly deformed shapes (Figure 10). These equilibrium shapes may be predicted using a geometrical limit where the membrane is unstretchable but can accommodate large compression through the formation of wrinkles (Paulsen et al. 2015). Depending on the amount of liquid present inside the structure, a circular sheet first adopts a shape analogous to the parachutes described by Taylor (1963). As

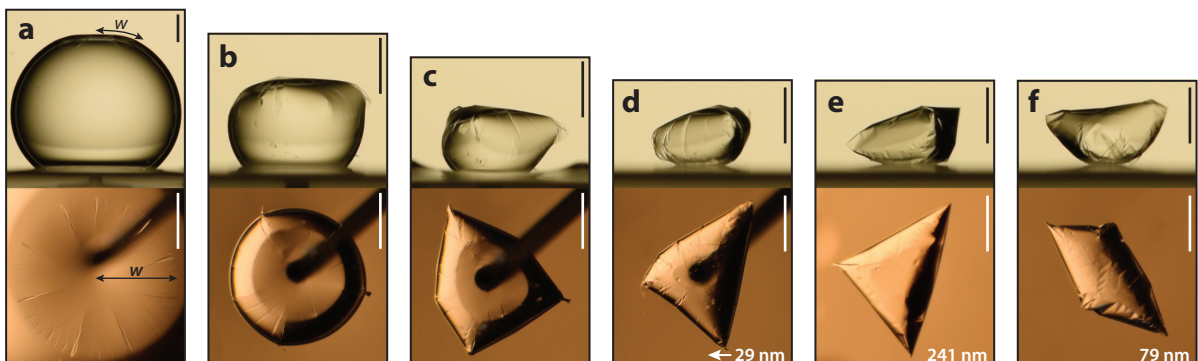


Figure 10

In the limit of very flexible sheets ($R \gg \ell_B$), capillary wrapping leads to geometrically optimal nonaxisymmetric shapes. All scale bars are 1 mm. Adapted from Paulsen et al. (2015).

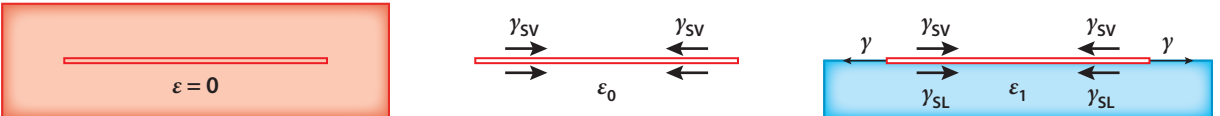


Figure 11

Action of surface stresses on a thin sheet: Whereas the ideal extraction of a membrane would induce a compressive strain ε_0 , depositing this membrane at the surface of a liquid bath results in a stretching strain ε_1 . Laying a thin sheet initially sustained in the air thus leads to a relative strain $\varepsilon = \varepsilon_1 - \varepsilon_0$. Nevertheless, the global tension across the membrane is equal to the surface tension of the liquid γ (γ_{SL} and γ_{SV} are the solid/liquid and solid/vapor interfacial tensions, respectively).

the volume of trapped liquid decreases, the global shape undergoes symmetry breaking, leading to structures reminiscent of samosas (Figure 10).

4.2. Capillary Stretching

The previous situations mostly involve a balance between capillary forces and bending. In this section, we examine if surface tension may induce significant stretching in an elastic membrane.

4.2.1. Stretching parameter. Consider a model configuration where a thin disk floats on the surface of a liquid bath (Figure 11c). We assume for simplicity that the surface energy of the solid does not depend on strain so that the notions of surface stress and energy presented in Section 2.1 are here equivalent. The total mechanical tension sustained by the membrane is the surface tension of the liquid γ , but surface stresses apply along the faces of the membrane, leading to an absolute in-plane strain, $\varepsilon_1 = (\gamma - \gamma_{SV} - \gamma_{SL})/Et$, where γ_{SV} and γ_{SL} are the solid/vapor and solid/liquid surface energies, respectively. This deformation takes as a reference state the solid without interfacial forces in a putative state where it would be surrounded by the same material (Figure 11a). In practice, however, one would measure this deformation with respect to a reference state corresponding to a membrane freely suspended in air (Figure 11b), therefore, with an absolute compression induced by the surface stress, $\varepsilon_0 = 2\gamma_{SV}/Et$. In conclusion, depositing the membrane at the surface of the liquid leads to the relative stretching strain:

$$\varepsilon = \varepsilon_1 - \varepsilon_0 = (1 + \cos \theta) \mathcal{S}, \quad 20.$$

where $\mathcal{S} = \gamma/Et$ and θ is the Young contact angle. The capillary-stretching parameter \mathcal{S} thus corresponds to the characteristic strain induced on a sheet by surface tension or, equivalently, to the ratio of surface tension to stretching energies.

In general, we therefore expect elastocapillary systems with a size L to depend on two dimensionless parameters, L/ℓ_B and \mathcal{S} . Typical values of \mathcal{S} used in the experiments reported in this review range from 10^{-3} to 10^{-6} , and it would be tempting to disregard stretching effects. Nevertheless, due to boundary conditions or to the geometry of the system, the impact of stretching and in-plane forces may be significant.

4.2.2. Capillary wrapping of a rigid sphere. A first illustration of capillary-induced stretching is the wrapping of a solid sphere by a thin sheet coated with a wetting liquid. Consider an ideal case where an initially flat disk of radius a and thickness t perfectly covers a sphere of radius R (Figure 12a). We focus here on the limit where bending is negligible compared to capillary adhesion ($R \gg \ell_B$). Transforming the disk into a spherical cap results in a radial extension and an orthoradial compression of the sheet. Indeed, keeping the perimeter of the disk constant as it is embossed to the sphere obviously tends to stretch the radial direction, and conversely, maintaining the diameter results in an excess of perimeter. The scaling for the corresponding strains can be

Capillary-stretching parameter: $\mathcal{S} = \frac{\gamma}{Et}$

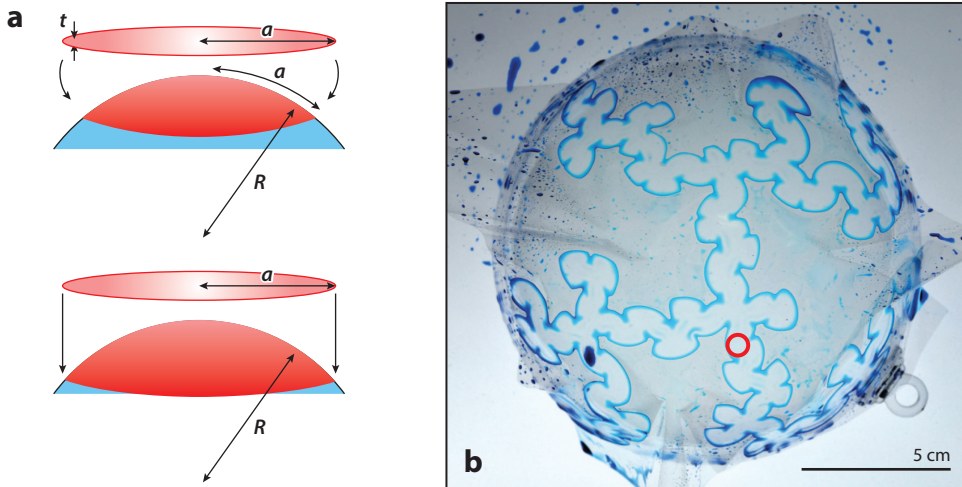


Figure 12

(a) Sticking a thin disk on a sphere faces geometrical incompatibilities: Maintaining a constant radius in the disk results in a compression of the perimeter, and conversely, maintaining a constant perimeter induces a stretching strain along the radial direction. (b) Depositing a wide adhesive sheet on a sphere leads to complex adhesion patterns whose width (diameter of the red circle) is set by the critical radius a_c .

estimated from simple length conservation as $\varepsilon \sim (a/R)^2$, which leads to a cost in elastic energy $\mathcal{U}_e \sim Eta^2(a/R)^4$. Conversely, the gain in adhesion energy simply reads $\mathcal{U}_s \sim \gamma a^2$. The disk is therefore expected to adhere perfectly on the sphere if its radius is below a critical value (Majidi & Adams 2009):

$$a_c = R \mathcal{S}^{1/4}. \quad 21.$$

Very complex adhesion patterns are experimentally obtained with larger disks (**Figure 12b**). However, the characteristic width of these patterns remains set by a_c (Hure et al. 2011).

An interesting transition between bending and stretching is also found in the liquid blister test (Chopin et al. 2008). A sheet is initially laid on a plate covered with a thin layer of liquid and indented from underneath through a hole in the plate. Different transitions are observed as the displacement d imposed by the indentor increases. First, the blister remains axisymmetric, and its extension R is dictated by a balance between stretching and adhesion and follows $R \sim d\mathcal{S}^{-1/4}$. However, due to the increasing stretching energy, the blister eventually takes a triangular shape set by a balance between bending and adhesion.

We see in these examples that capillary adhesion leads to in-plane stresses that are the main determinants of the boundaries of adhesive patches. These stresses are not due to the capillary force directly pulling on the boundary of the plate, but are indirectly induced by the distortion in its geometry.

4.2.3. Sheet on a drop. We now describe another scenario for capillary stretching. In an elegant experiment (**Figure 13a**), a very thin polymeric disk of radius L is laid on a liquid drop of radius $R \gg \ell_B$ (King et al. 2012). The combination of capillary traction along the boundary and Laplace pressure acting on the surface of the sheet tends to impose the radius of curvature of the droplet on the elastic disk, leading to radial tension and orthoradial compression, as in the case of the rigid sphere. Consequently, wrinkles appear when the compressive stress induced by the deformation of the disk overcomes the capillary tension: $Et(L/R)^2 \sim \gamma$ (i.e., $L/R \sim \mathcal{S}^{1/2}$). The wavelength of

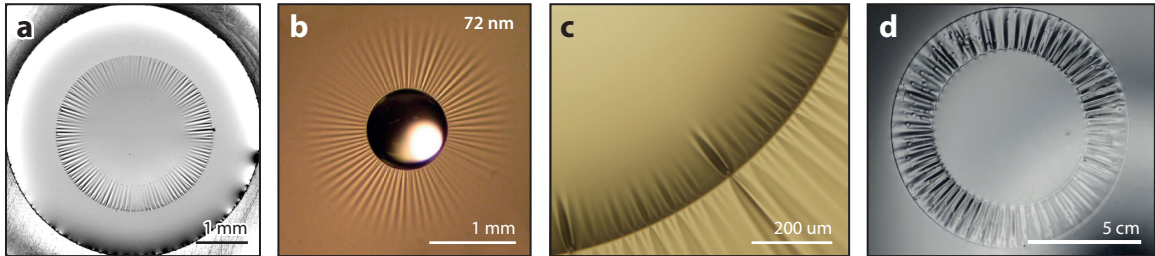


Figure 13

(*a*) A disk of very flexible membrane wrinkles when laid on a drop (King et al. 2012). (*b*) A drop or a bubble on a very flexible floating membrane generates tension that leads to wrinkling (Huang et al. 2007). (*c*) A close-up view of the vicinity of the contact line reveals a complex cascade of wrinkles on both sides of the contact line (Toga et al. 2013). (*d*) Wrinkles are also observed on a floating annulus subject to differential surface tension (Piñeirua et al. 2013).

the wrinkles results from a balance between capillary traction and bending stiffness (Paulsen et al. 2016). When the radius of the sphere decreases (and therefore the compressive orthoradial load increases), localized folds eventually appear and their description motivates current theoretical developments.

4.2.4. Drop on a floating sheet. Another elastocapillary experiment consists of depositing a tiny drop on a large, thin disk floating on a liquid bath (Figure 13*b*). In the regime of highly compliant sheets (where the radius of the drop $R \gg \ell_B$), an intriguing radial wrinkling pattern is observed (Bodiguel 2006, Huang et al. 2007, Toga et al. 2013). As in the case described above, capillary forces produce a dimple in the sheet below the droplet, which results in radial tension. Outside the drop, this tension tends to pull inwards any material circle on the sheet, resulting in azimuthal compression. Wrinkling occurs when compression overcomes the isotropic tension initially induced by capillary traction on the outer boundaries of the floating membrane. Whereas the number N of wrinkles apparently relies on a balance between capillary traction and bending ($N \sim \sqrt{R/\ell_B}$), the interplay between surface tension and stretching dictates their radial extension L_w , as experiments were first interpreted to follow $L_w \sim RS^{-1/2}$ (Huang et al. 2007). From these two visual observations (N, L_w), one can infer ℓ_B and S and therefore nondestructively estimate both the material stiffness E and the thickness of the sheet t . This experiment triggered active research in recent years because the detailed description of the different phenomena is quite subtle. For example, note the period-doubling wrinkling close to the contact line with the drop (Figure 13*c*), which is reminiscent of the more complete capillary cascade observed by Huang et al. (2010). Only after several years did theoretical studies obtain a prediction for the extension, $L_w \sim RS^{-1/3}$, which would also be compatible with experimental data (Schroll et al. 2013).

In an attempt to understand this capillary wrinkling, researchers first considered the simpler situation of an annulus floating on water: Wrinkling appears when the surface tension of the outer liquid γ_o is significantly lower than that of the inner liquid surface γ_i (for instance, if surfactant is added outside the annulus). Indeed, the stronger inner tension γ_i tends to reduce the radius of the inner hole, leading to azimuthal compression of the annulus along its inner boundary and, eventually, to buckling. A first experimental realization of this problem in a macroscopic system (Piñeirua et al. 2013) was limited to a different regime, where the buckling wavelength was determined by the interplay of bending rigidity and underlying liquid weight (Figure 13*d*). However, in the limit of infinitely flexible sheets, or $R/\ell_B \ll 1$, theory shows that wrinkles extend over a distance $L_w = R\gamma_i/2\gamma_o$, where R is the radius of the inner hole in an infinite

membrane (Davidovitch et al. 2011). When returning to the initial problem of the drop on a sheet, this result was used with the drop-induced pulling stresses γ_i , which were estimated as $\gamma_i^3 \sim Et \gamma_o^2$ in the limit of infinitely flexible sheets, leading to $L_w \sim R(Et/\gamma_o)^{1/3} \sim RS^{-1/3}$. However, the richness of the simplified problem is illustrated by recent experiments using ultrathin sheets, which showed that far above the buckling threshold, a partial collapse of a finite annulus may also occur (Paulsen et al. 2017).

If the liquid drop is deposited on a very thin elastomer membrane clamped along its remote boundary, the drop strongly deforms the membrane (Schulman & Dalnoki-Veress 2015), seen as an extremely compliant substrate. From the observation of the apparent contact angles, one can measure the tension in the membrane, allowing one to infer the surface stress of the elastomer (Nadermann et al. 2013). Droplets deposited on opposite sides of the membranes interact through the out-of-plane deformation of the membrane that they induce and therefore spontaneously assemble (Liu et al. 2017).

5. CONCLUSION

Although surface tension is usually not considered in fluid–structure interactions involving large scales, capillary forces become dominant at the submillimetric scale and may deform micro-objects. In this review, we focus on three main types of deformation occurring at different dimensions. 3D deformations of an elastic solid induced by capillarity occur at a shear elastocapillary length $\ell_s \sim \Upsilon/G$. The parameter Υ represents the surface stress acting at the surface of a solid in the case of an object immersed in a fluid. It can also be taken as the surface tension of a liquid γ when the deformations induced by a sessile droplet at the surface of a solid are considered. Because this length scale is atomic for usual engineering materials, elastocapillary phenomena have long been neglected. However, the growing development of soft polymers provides access to materials with Young’s moduli 5–10 orders of magnitude smaller than steel, paving the way for stimulating studies on elastocapillarity at the macroscopic scale.

Bending, buckling, bundling, or coiling deformations in 1D slender structures produce spectacular shapes and patterns. The typical curvature induced by surface tension forces may be described by the bending length $\ell_B \sim \sqrt{Et^3}/\gamma$, where Et^3 is the bending modulus for a structure of thickness t .

The bending of slender structures may be extended to 2D sheets. However, geometrical constraints result in stretching and compression, which may lead to complex buckling instabilities and beautiful patterns such as wrinkles or folds. The effect of stretching/compression is characterized by a stretching parameter $S = \gamma/Et$, which can also be viewed as the comparison of ℓ_s with the thickness of the structure.

In conclusion, elastocapillarity describes fascinating phenomena across many length scales. It covers a wide range of academic and applied problems from static and dynamic wetting and adhesion to the self-assembly of slender structures or the generation of 3D shapes from flat templates. Biophysics—a field driven by better mechanical control at the cellular level—is particularly ripe for numerous upcoming applications. For instance, Campàs et al. (2013) nicely demonstrate how capillary pressure may be used for *in vivo* probing of living cells. Tubes of biological membranes are also known to undergo an instability reminiscent of the elastocapillary instability of soft gels, which leads to the fragmentation of mitochondria through pearlizing (Gonzalez-Rodriguez et al. 2015). The development of micro- and nanoengineered mechanical devices is also likely to raise new elastocapillary problems.

SUMMARY POINTS

1. The 3D deformation of a bulk solid induced by surface tension occurs at the shear length scale $\ell_S = \Upsilon/G$. This scale is atomic for traditional engineering materials but may become macroscopic when soft polymeric or biological materials are involved.
2. Depositing a liquid droplet at the surface of a soft elastic solid induces the formation of a wetting ridge of typical extension ℓ_S , which affects the static and dynamic wetting properties of the liquid.
3. Capillary-induced moments may bend 1D slender structures. The corresponding curvature is dictated by a bending length $\ell_B \sim \sqrt{Et^3/\gamma}$.
4. This bending effect may be extended to 2D sheets or shells, although geometrical constraints may induce the stretching or compression of the structure. This additional effect is characterized by a stretching number $\mathcal{S} = \gamma/Et$.

FUTURE ISSUES

1. Depositing a liquid droplet on a soft substrate induces the formation of a ridge of typical size ℓ_S . However, the physical cutoffs of the stress singularities at the contact line remain to be confirmed. Most soft materials are composed of polymers or gels, and the evolution of surface stresses with strain is not obvious. Determining such stresses experimentally is also important because a strong variation of Υ in the vicinity of the ridge should modify its profile. More generally, understanding the dynamics of the deformation of soft solids is crucial. Measuring the dynamics of a droplet sliding on a soft substrate may indeed constitute a rheometry technique to probe soft materials.
2. Two different mechanisms seem to explain the formation of bundles obtained experimentally with arrays of wet fibers. However, the range of application of these scenarios remains to be confirmed. More generally, understanding the bundling dynamics would be very valuable. Several works have been dedicated to flexible rods, but the general case of 2D arrays of fibers remains an open question.
3. Although the large-amplitude deformation of thin sheets mainly relies on bending, stretching and compression may also play an important role due to geometrical incompatibilities. A consequence of this additional ingredient is the formation of wrinkles, folds, or crumples, especially in the case of very thin sheets or shells (of size $L \gg \ell_B$). The description of such complex structures deserves a comprehensive review. Beyond static shapes, understanding the wrapping dynamics is also important from a practical point of view, because the final structure may rely on the order of the folding events.
4. Finally, building on the framework of elastocapillary phenomena may pave the way for the exploration of other surface interactions such as adhesion and even fracture, which can also be described in terms of surface energy. Nevertheless, additional effects such as friction may have to be added.

DISCLOSURE STATEMENT

The authors are not aware of any biases that might be perceived as affecting the objectivity of this review.

ACKNOWLEDGMENTS

We thank Étienne Guyon for the useful comments on our manuscript. This work was partly funded by the Interuniversity Attraction Poles Programme (IAP 7/38 MicroMAST) initiated by the Belgian Science Policy Office and the Fonds National de la Recherche Scientifique.

LITERATURE CITED

- Abe T, Reed ML. 1996. Control of liquid bridging induced stiction of micromechanical structures. *J. Micromech. Microeng.* 6:213–17
- Adami N, Caps H. 2015. Surface tension profiles in vertical soap films. *Phys. Rev. E* 91:013007
- Alizadeh A, Bahadur V, Shang W, Zhu Y, Buckley D, et al. 2013. Influence of substrate elasticity on droplet impact dynamics. *Langmuir* 29:4520–24
- Andreotti B, Bäumchen O, Boulogne F, Daniels KE, Dufresne ER, et al. 2016. Solid capillarity: When and how does surface tension deform soft solids? *Soft Matter* 12:2993–96
- Andreotti B, Marchand A, Das S, Snoeijer JH. 2011. Elastocapillary instability under partial wetting conditions: bending versus buckling. *Phys. Rev. E* 84:061601
- Andreotti B, Snoeijer JH. 2016. Soft wetting and the Shuttleworth effect, at the crossroads between thermodynamics and mechanics. *Europhys. Lett.* 113:66001
- Anoop R, Sen AK. 2015. Capillary flow enhancement in rectangular polymer microchannels with a deformable wall. *Phys. Rev. E* 92:013024
- Antkowiak A, Audoly B, Josserand C, Neukirch S, Rivetti M. 2011. Instant fabrication and selection of folded structures using drop impact. *PNAS* 108:10400–4
- Aristoff JM, Duprat C, Stone HA. 2011. Elastocapillary imbibition. *Int. J. Non-Linear Mech.* 46:648–56
- Audoly B, Pomeau Y. 2010. *Elasticity and Geometry: From Hair Curls to the Non-Linear Response of Shells*. Oxford, UK: Oxford Univ. Press
- Bae J, Ouchi T, Hayward RC. 2015. Measuring the elastic modulus of thin polymer sheets by elastocapillary bending. *ACS Appl. Mater. Interfaces* 7:14734–42
- Barrière B, Sekimoto K, Leibler L. 1996. Peristaltic instability of cylindrical gels. *J. Chem. Phys.* 105:1735–38
- Bernardino NR, Dietrich S. 2012. Complete wetting of elastically responsive substrates. *Phys. Rev. E* 85:051603
- Bico J, Roman B, Moulin L, Boudaoud A. 2004. Adhesion: elastocapillary coalescence in wet hair. *Nature* 432:690
- Bodiguel H. 2006. *Propriétés mécaniques de films polymères ultraminces*. PhD Thesis, Univ. Paris VI
- Bonacurso E, Butt HJ. 2005. Microdrops on atomic force microscope cantilevers: evaporation of water and spring constant calibration. *J. Phys. Chem. B* 109:253–63
- Boncheva M, Whitesides GM. 2005. Making things by self-assembly. *MRS Bull.* 30:736–42
- Boudaoud A, Bico J, Roman B. 2007. Elastocapillary coalescence: aggregation and fragmentation with a maximal size. *Phys. Rev. E* 76:060102
- Brubaker ND, Lega J. 2016a. Capillary-induced deformations of a thin elastic sheet. *Philos. Trans. R. Soc. A* 374:20150169
- Brubaker ND, Lega J. 2016b. Two-dimensional capillary origami. *Phys. Lett. A* 380:83–87
- Cambau T, Bico J, Reyssat E. 2011. Capillary rise between flexible walls. *Europhys. Lett.* 96:24001
- Campàs O, Mammoto T, Hasso S, Sperling RA, O’Connell D, et al. 2013. Quantifying cell-generated mechanical forces within living embryonic tissues. *Nat. Methods* 11:183–89

- Carré A, Gastel JC, Shanahan MER. 1996. Viscoelastic effects in the spreading of liquids. *Nature* 379:432–34
- Chakrapani N, Wei B, Carrillo A, Ajayan PM, Kane RS. 2004. Capillarity-driven assembly of two-dimensional cellular carbon nanotube foams. *PNAS* 101:4009–12
- Chandra D, Yang S. 2009. Capillary-force-induced clustering of micropillar arrays: Is it caused by isolated capillary bridges or by the lateral capillary meniscus interaction force? *Langmuir* 25:10430–34
- Chandra D, Yang S. 2010. Stability of high-aspect-ratio micropillar arrays against adhesive and capillary forces. *Acc. Chem. Res.* 43:1080–91
- Chaudhury MK, Weaver T, Hui CY, Kramer EJ. 1996. Adhesive contact of cylindrical lens and a flat sheet. *J. Appl. Phys.* 80:30–37
- Chen D, Cai S, Suo Z, Hayward RC. 2012. Surface energy as a barrier to creasing of elastomer films: an elastic analogy to classical nucleation. *Phys. Rev. Lett.* 109:038001
- Chen L, Wang X, Wen W, Li Z. 2010. Critical droplet volume for spontaneous capillary wrapping. *Appl. Phys. Lett.* 97:124103
- Chiodi F, Roman B, Bico J. 2010. Piercing an interface with a brush: collaborative stiffening. *Europhys. Lett.* 90:44006
- Cho J-H, Gracias DH. 2009. Self-assembly of lithographically patterned nanoparticles. *Nano Lett.* 9:4049–52
- Chopin J, Vella D, Boudaoud A. 2008. The liquid blister test. *Proc. R. Soc. A* 464:2887–906
- Cohen AE, Mahadevan L. 2003. Kinks, rings, and rackets in filamentous structures. *PNAS* 100:12141–46
- Correa-Duarte MA, Wagner N, Rojas-Chapana J, Morszeck C, Thie M, Giersig M. 2004. Fabrication and biocompatibility of carbon nanotube-based 3D networks as scaffolds for cell seeding and growth. *Nano Lett.* 4:2233–36
- Crane NB, Onen O, Carballo J, Ni Q, Guldiken R. 2013. Fluidic assembly at the microscale: progress and prospects. *Microfluid. Nanofluid.* 14:383–419
- Cuenot S, Fréty C, Demoustier-Champagne S, Nysten B. 2004. Surface tension effect on the mechanical properties of nanomaterials measured by atomic force microscopy. *Phys. Rev. B* 69:165410
- Das S, Marchand A, Andreotti B, Snoeijer JH. 2011. Elastic deformation due to tangential capillary forces. *Phys. Fluids* 23:072006
- Davidovitch B, Schroll RD, Vella D, Adda-Bedia M, Cerdá EA. 2011. Prototypical model for tensional wrinkling in thin sheets. *PNAS* 108:18227–32
- de Gennes PG, Brochard-Wyart F, Quéré D. 2004. *Capillarity and Wetting Phenomena*. New York: Springer
- de Langre E, Baroud C, Reverdy P. 2010. Energy criteria for elasto-capillary wrapping. *J. Fluids Struct.* 26:205–17
- De Volder M, Hart AJ. 2013. Engineering hierarchical nanostructures by elastocapillary self-assembly. *Angew. Chem. Int. Ed.* 52:2412–25
- De Volder M, Tawfick SH, Park SJ, Copic D, Zhao Z, et al. 2010. Diverse 3D microarchitectures made by capillary forming of carbon nanotubes. *Adv. Mater.* 22:4384–89
- De Volder M, Tawfick SH, Park SJ, Hart AJ. 2011. Corrugated carbon nanotube microstructures with geometrically tunable compliance. *ACS Nano* 5:7310–17
- DelRio FW, de Boer MP, Knapp JA, Reedy ED, Clews PJ, Dunn ML. 2005. The role of van der Waals forces in adhesion of micromachined surfaces. *Nat. Mater.* 4:629–34
- Duan H, Berggren KK. 2010. Directed self-assembly at the 10 nm scale by using capillary force-induced nanocohesion. *Nano Lett.* 10:3710–16
- Ducloué L, Hazel AL, Thompson AB, Juel A. 2017. Reopening modes of a collapsed elasto-rigid channel. *J. Fluid Mech.* 819:121–46
- Ducloué L, Pitois O, Goyon J, Chateau X, Ovarlez G. 2014. Coupling of elasticity to capillarity in soft aerated materials. *Soft Matter* 10:5093–98
- Duprat C, Aristoff JM, Stone HA. 2011. Dynamics of elastocapillary rise. *J. Fluid Mech.* 679:641–54
- Duprat C, Protière S. 2015. Capillary stretching of fibers. *Europhys. Lett.* 111:56006
- Duprat C, Protière S, Beebe AY, Stone HA. 2012. Wetting of flexible fibre arrays. *Nature* 482:510–13

- Duprat C, Stone H, eds. 2015. *Fluid–Structure Interactions in Low-Reynolds-Number Flows*. Cambridge, UK: R. Soc. Chem.
- Eletro H, Neukirch S, Vollrath F, Antkowiak A. 2016. In-drop capillary spooling of spider capture thread inspires hybrid fibers with mixed solid–liquid mechanical properties. *PNAS* 113:6143–47
- Eshelby JD. 1957. The determination of the elastic field of an ellipsoidal inclusion, and related problems. *Proc. R. Soc. A* 241:376–96
- Extrand C, Kumagai Y. 1996. Contact angles and hysteresis on soft surfaces. *J. Colloid Interface Sci.* 184:191–200
- Fargette A, Neukirch S, Antkowiak A. 2014. Elastocapillary snapping: Capillarity induces snap-through instabilities in small elastic beams. *Phys. Rev. Lett.* 112:137802
- Fei Y, Maia HT, Batty C, Zheng C, Grinshpun E. 2017. A multi-scale model for simulating liquid-hair interactions. *ACM Trans. Graph.* 36:56
- Fernandes R, Gracias DH. 2012. Self-folding polymeric containers for encapsulation and delivery of drugs. *Adv. Drug Deliv. Rev.* 64:1579–89
- Filipiak DJ, Azam A, Leong TG, Gracias DH. 2009. Hierarchical self-assembly of complex polyhedral microcontainers. *J. Micromech. Microeng.* 19:075012
- García EJ, Hart AJ, Wardle BL, Slocum AH. 2007. Fabrication of composite microstructures by capillarity-driven wetting of aligned carbon nanotubes with polymers. *Nanotechnology* 18:165602
- Geraldi NR, Ouali FF, Morris RH, McHale G, Newton MI. 2013. Capillary origami and superhydrophobic membrane surfaces. *Appl. Phys. Lett.* 102:214104
- Gernay S, Federle W, Lambert P, Gilet T. 2016. Elasto-capillarity in insect fibrillar adhesion. *J. R. Soc. Interface* 13:20160371
- Gonzalez-Rodriguez D, Sart S, Babataheri A, Tareste D, Barakat AI, et al. 2015. Elastocapillary instability in mitochondrial fission. *Phys. Rev. Lett.* 115:088102
- Grotberg JB, Jensen OE. 2004. Biofluid mechanics in flexible tubes. *Annu. Rev. Fluid Mech.* 36:121–47
- Guo X, Li H, Ahn BY, Duoss EB, Hsia KJ, et al. 2009. Two- and three-dimensional folding of thin film single-crystalline silicon for photovoltaic power applications. *PNAS* 106:20149–54
- Hadjitofis A, Lister JR, Singh K, Vella D. 2016. Evaporation effects in elastocapillary aggregation. *J. Fluid Mech.* 792:168–85
- Hazel AL, Heil M. 2003. Three-dimensional airway reopening: the steady propagation of a semi-infinite bubble into a buckled elastic tube. *J. Fluid Mech.* 478:47–70
- Henann DL, Bertoldi K. 2014. Modeling of elasto-capillary phenomena. *Soft Matter* 10:709–17
- Howland CJ, Antkowiak A, Castrejón-Pita JR, Howison SD, Oliver JM, et al. 2016. It's harder to splash on soft solids. *Phys. Rev. Lett.* 117:184502
- Hu M, Ou FS, Wu W, Naumov I, Li X, et al. 2010. Gold nanofingers for molecule trapping and detection. *J. Am. Chem. Soc.* 132:12820–22
- Hu Y, Lao Z, Cumming BP, Wu D, Li J, et al. 2015. Laser printing hierarchical structures with the aid of controlled capillary-driven self-assembly. *PNAS* 112:6876–81
- Hu Y, Lee KYC, Israelachvili J. 2003. Sealed minitrough for microscopy and long-term stability studies of Langmuir monolayers. *Langmuir* 19:100–4
- Huang J, Davidovitch B, Santangelo CD, Russell TP, Menon N. 2010. Smooth cascade of wrinkles at the edge of a floating elastic film. *Phys. Rev. Lett.* 105:038302
- Huang J, Juszkiewicz M, de Jeu WH, Cerdá E, Emrick T, et al. 2007. Capillary wrinkling of floating thin polymer films. *Science* 317:650–53
- Hui CY, Jagota A, Lin YY, Kramer EJ. 2002. Constraints on microcontact printing imposed by stamp deformation. *Langmuir* 18:1394–407
- Hure J, Roman B, Bico J. 2011. Wrapping an adhesive sphere with an elastic sheet. *Phys. Rev. Lett.* 106:174301
- Jagota A, Paretkar D, Ghatak A. 2012. Surface-tension-induced flattening of a nearly plane elastic solid. *Phys. Rev. E* 85:051602
- Jamin T, Py C, Falcon E. 2011. Instability of the origami of a ferrofluid drop in a magnetic field. *Phys. Rev. Lett.* 107:204503
- Jerison ER, Xu Y, Wilen LA, Dufresne ER. 2011. Deformation of an elastic substrate by a three-phase contact line. *Phys. Rev. Lett.* 106:186103

- Kajiya T, Daerr A, Narita T, Royon L, Lequeux F, Limat L. 2013. Advancing liquid contact line on visco-elastic gel substrates: stick-slip versus continuous motions. *Soft Matter* 9:454–61
- Kang SH, Pokroy B, Mahadevan L, Aizenberg J. 2010. Control of shape and size of nanopillar assembly by adhesion-mediated elastocapillary interaction. *ACS Nano* 4:6323–31
- Karpitschka S, Das S, van Gorcum M, Perrin H, Andreotti B, Snoeijer JH. 2015. Droplets move over viscoelastic substrates by surfing a ridge. *Nat. Commun.* 6:7891
- Karpitschka S, Pandey A, Lubbers LA, Wijs JH, Botto L, et al. 2016. Liquid drops attract or repel by the inverted Cheerios effect. *PNAS* 113:7403–7
- Kern R, Müller P. 1992. Deformation of an elastic thin solid induced by a liquid droplet. *Surf. Sci.* 264:467–94
- Kim HY, Mahadevan L. 2006. Capillary rise between elastic sheets. *J. Fluid Mech.* 548:141–50
- Kim TH, Kim J, Kim Hy. 2016. Evaporation-driven clustering of microscale pillars and lamellae. *Phys. Fluids* 28:022003
- King H, Schroll RD, Davidovitch B, Menon N. 2012. Elastic sheet on a liquid drop reveals wrinkling and crumpling as distinct symmetry-breaking instabilities. *PNAS* 109:9716–20
- Kralchevsky PA, Nagayama K. 2000. Capillary interactions between particles bound to interfaces, liquid films and biomembranes. *Adv. Colloid Interface Sci.* 85:145–92
- Lau KKS, Bico J, Teo KBK, Chhowalla M, Amarasingha GAJ, et al. 2003. Superhydrophobic carbon nanotube forests. *Nano Lett.* 3:1701–5
- Legrain A, Berenschot EJW, Abelmann L, Bico J, Tas NR. 2016. Let's twist again: elasto-capillary assembly of parallel ribbons. *Soft Matter* 12:7186–94
- Legrain A, Janson TG, Berenschot JW, Abelmann L, Tas NR. 2014. Controllable elastocapillary folding of three-dimensional micro-objects by through-wafer filling. *J. Appl. Phys.* 115:214905
- Leong TG, Zarafshar AM, Gracias DH. 2010. Three-dimensional fabrication at small size scales. *Small* 6:792–806
- Lester G. 1961. Contact angles of liquids at deformable solid surfaces. *J. Colloid Sci.* 16:315–26
- Liang H, Cao Z, Dobrynin AV. 2016. Molecular dynamics simulations of the effect of elastocapillarity on reinforcement of soft polymeric materials by liquid inclusions. *Macromolecules* 49:7108–15
- Limat L. 2012. Straight contact lines on a soft, incompressible solid. *Eur. Phys. J. E* 35:134
- Liu T, Xu X, Nadermann N, He Z, Jagota A, Hui CY. 2017. Interaction of droplets separated by an elastic film. *Langmuir* 33:75–81
- Long D, Ajdari A, Leibler L. 1996. Static and dynamic wetting properties of thin rubber films. *Langmuir* 12:5221–30
- Maboudian R. 1997. Critical review: adhesion in surface micromechanical structures. *J. Vac. Sci. Technol. B* 15:1–20
- Majidi C, Adams GG. 2009. A simplified formulation of adhesion problems with elastic plates. *Proc. R. Soc. A* 465:2217–30
- Manakasettharn S, Taylor JA, Krupenkin TN. 2011. Bio-inspired artificial iridophores based on capillary origami: fabrication and device characterization. *Appl. Phys. Lett.* 99:144102
- Marchand A, Das S, Snoeijer JH, Andreotti B. 2012. Contact angles on a soft solid: from Young's law to Neumann's law. *Phys. Rev. Lett.* 109:236101
- Martel R, Shea HR, Avouris P. 1999. Ring formation in single-wall carbon nanotubes. *J. Phys. Chem. B* 103:7551–56
- Mastrangeli M, Abbasi S, Varel C, Van Hoof C, Celis JP, Böhringer KF. 2009. Self-assembly from milli- to nanoscales: methods and applications. *J. Micromech. Microeng.* 19:083001
- Matsuo ES, Tanaka T. 1992. Patterns in shrinking gels. *Nature* 358:482–85
- Mehrabian H, Harting J, Snoeijer JH. 2016. Soft particles at a fluid interface. *Soft Matter* 12:1062–73
- Meng Q, Wang Q, Liu H, Jiang L. 2014. A bio-inspired flexible fiber array with an open radial geometry for highly efficient liquid transfer. *NPG Asia Mater.* 6:e125
- Mora S, Abkarian M, Tabuteau H, Pomeau Y. 2011. Surface instability of soft solids under strain. *Soft Matter* 7:10612–19

- Mora S, Maurini C, Phou T, Fromental JM, Audoly B, Pomeau Y. 2013. Solid drops: large capillary deformations of immersed elastic rods. *Phys. Rev. Lett.* 111:114301
- Mora S, Phou T, Fromental JM, Pismen LM, Pomeau Y. 2010. Capillarity driven instability of a soft solid. *Phys. Rev. Lett.* 105:214301
- Mora S, Pomeau Y. 2015. Softening of edges of solids by surface tension. *J. Phys. Condens. Matter* 27:194112
- Nadermann N, Hui CY, Jagota A. 2013. Solid surface tension measured by a liquid drop under a solid film. *PNAS* 110:10541–45
- Neukirch S, Roman B, de Gaudemaris B, Bico J. 2007. Piercing a liquid surface with an elastic rod: buckling under capillary forces. *J. Mech. Phys. Solids* 55:1212–35
- Nicolson MM. 1955. Surface tension in ionic crystals. *Proc. R. Soc. A* 228:490–510
- Olives J. 1993. Capillarity and elasticity. The example of the thin plate. *J. Phys. Condens. Matter* 5:2081–94
- Paretkar D, Xu X, Hui CY, Jagota A. 2014. Flattening of a patterned compliant solid by surface stress. *Soft Matter* 10:4084–90
- Park SJ, Schmidt AJ, Tawfick SH, Hart AJ. 2014. Precise control of elastocapillary densification of nanostructures via low-pressure condensation. *J. Micromech. Microeng.* 24:065019
- Patra N, Wang B, Kral P. 2009. Nanodroplet activated and guided folding of graphene nanostructures. *Nano Lett.* 9:3766–71
- Paulsen JD, Démery V, Santangelo CD, Russell TP, Davidovitch B, Menon N. 2015. Optimal wrapping of liquid droplets with ultrathin sheets. *Nat. Mater.* 14:1206–9
- Paulsen JD, Démery V, Toga KB, Qiu Z, Russell TP, et al. 2017. Geometry-driven folding of a floating annular sheet. *Phys. Rev. Lett.* 118:048004
- Paulsen JD, Hohlfeld E, King H, Huang J, Qiu Z, et al. 2016. Curvature-induced stiffness and the spatial variation of wavelength in wrinkled sheets. *PNAS* 113:1144–49
- Péraud JP, Lauga E. 2014. Geometry and wetting of capillary folding. *Phys. Rev. E* 89:043011
- Pericet-Camara R, Best A, Butt HJ, Bonaccurso E. 2008. Effect of capillary pressure and surface tension on the deformation of elastic surfaces by sessile liquid microdrops: an experimental investigation. *Langmuir* 24:10565–68
- Pham JT, Lawrence J, Lee DY, Grason GM, Emrick T, Crosby AJ. 2013. Highly stretchable nanoparticle helices through geometric asymmetry and surface forces. *Adv. Mater.* 25:6703–8
- Piñeirua M, Bico J, Roman B. 2010. Capillary origami controlled by an electric field. *Soft Matter* 6:4491–96
- Piñeirua M, Tanaka N, Roman B, Bico J. 2013. Capillary buckling of a floating annulus. *Soft Matter* 9:10985–92
- Pokroy B, Kang SH, Mahadevan L, Aizenberg J. 2009. Self-organization of a mesoscale bristle into ordered, hierarchical helical assemblies. *Science* 323:237–40
- Py C, Bastien R, Bico J, Roman B, Boudaoud A. 2007a. 3D aggregation of wet fibers. *Europhys. Lett.* 77:44005
- Py C, Reverdy P, Doppler L, Bico J, Roman B, Baroud CN. 2007b. Capillary origami: spontaneous wrapping of a droplet with an elastic sheet. *Phys. Rev. Lett.* 98:156103
- Reis PM, Hure J, Jung S, Bush JWM, Clanet C. 2010. Grabbing water. *Soft Matter* 6:5705–8
- Rico-Guevara A, Rubega MA. 2011. The hummingbird tongue is a fluid trap, not a capillary tube. *PNAS* 108:9356–60
- Rivetti M, Neukirch S. 2012. Instabilities in a drop-strip system: a simplified model. *Proc. R. Soc. A* 468:1304–24
- Roca-Cusachs P, Rico F, Martínez E, Toset J, Farré R, Navajas D. 2005. Stability of microfabricated high aspect ratio structures in poly(dimethylsiloxane). *Langmuir* 21:5542–48
- Roman B, Bico J. 2010. Elasto-capillarity: deforming an elastic structure with a liquid droplet. *J. Phys. Condens. Matter* 22:493101
- Rusanov A. 1978. On the thermodynamics of deformable solid surfaces. *J. Colloid Interface Sci.* 63:330–45
- Salez T, Benzaquen M, Raphaël E. 2013. From adhesion to wetting of a soft particle. *Soft Matter* 9:10699–704
- Schroll RD, Adda-Bedia M, Cerdá E, Huang J, Menon N, et al. 2013. Capillary deformations of bendable films. *Phys. Rev. Lett.* 111:014301

- Schulman RD, Dalnoki-Veress K. 2015. Liquid droplets on a highly deformable membrane. *Phys. Rev. Lett.* 115:206101
- Schulman RD, Porat A, Charlesworth K, Fortais A, Salez T, et al. 2017. Elastocapillary bending of microfibers around liquid droplets. *Soft Matter* 13:720–24
- Shanahan MER. 1987. The influence of solid micro-deformation on contact angle equilibrium. *J. Phys. D Appl. Phys.* 20:945–50
- Shanahan MER. 1988. The spreading dynamics of a liquid drop on a viscoelastic solid. *J. Phys. D Appl. Phys.* 21:981–85
- Sharp KG, Blackman GS, Glassmaker NJ, Jagota A, Hui CY. 2004. Effect of stamp deformation on the quality of microcontact printing: theory and experiment. *Langmuir* 20:6430–38
- Singh K, Lister JR, Vella D. 2014. A fluid-mechanical model of elastocapillary coalescence. *J. Fluid Mech.* 745:621–46
- Snoeijer JH. 2016. Analogies between elastic and capillary interfaces. *Phys. Rev. Fluids* 1:060506
- Sokuler M, Auernhammer GK, Roth M, Liu C, Bonacurso E, Butt HJ. 2010. The softer the better: fast condensation on soft surfaces. *Langmuir* 26:1544–47
- Style RW, Boltynskiy R, Che Y, Wettlaufer JS, Wilen LA, Dufresne ER. 2013a. Universal deformation of soft substrates near a contact line and the direct measurement of solid surface stresses. *Phys. Rev. Lett.* 110:066103
- Style RW, Che Y, Park SJ, Weon BM, Je JH, et al. 2013b. Patterning droplets with durotaxis. *PNAS* 110:12541–44
- Style RW, Dufresne ER. 2012. Static wetting on deformable substrates, from liquids to soft solids. *Soft Matter* 8:7177–84
- Style RW, Hyland C, Boltynskiy R, Wettlaufer JS, Dufresne ER. 2013c. Surface tension and contact with soft elastic solids. *Nat. Commun.* 4:2728
- Style RW, Jagota A, Hui CY, Dufresne ER. 2017. Elastocapillarity: surface tension and the mechanics of soft solids. *Annu. Rev. Condens. Matter Phys.* 8:99–118
- Style RW, Wettlaufer JS, Dufresne ER. 2015. Surface tension and the mechanics of liquid inclusions in compliant solids. *Soft Matter* 11:672–79
- Syms R, Yeatman E, Bright V, Whitesides G. 2003. Surface tension-powered self-assembly of microstructures—the state-of-the-art. *J. Microelectromech. Syst.* 12:387–417
- Taffetani M, Ciarletta P. 2015. Elastocapillarity can control the formation and the morphology of beads-on-string structures in solid fibers. *Phys. Rev. E* 91:032413
- Taroni M, Vella D. 2012. Multiple equilibria in a simple elastocapillary system. *J. Fluid Mech.* 712:273–94
- Tas N, Sonnenberg T, Jansen H, Legtenberg R, Elwenspoek M. 1996. Stiction in surface micromachining. *J. Micromech. Microeng.* 6:385–97
- Tawfick SH, Bico J, Barcelo S. 2016. Three-dimensional lithography by elasto-capillary engineering of filamentary materials. *MRS Bull.* 41:108–14
- Taylor G. 1963. On the shapes of parachutes. In *The Scientific Papers of Sir Geoffrey Ingram Taylor*, Vol. 3, ed. GK Batchelor, pp. 26–37. Cambridge, UK: Cambridge Univ. Press
- Toga KB, Huang J, Cunningham K, Russell TP, Menon N. 2013. A drop on a floating sheet: boundary conditions, topography and formation of wrinkles. *Soft Matter* 9:8289–96
- Vollrath F, Edmonds DT. 1989. Modulation of the mechanical properties of spider silk by coating with water. *Nature* 340:305–7
- Wang K-Y, Chou C-H, Liao C-Y, Li Y-R, Cheng H-C. 2016. Densification effects of the carbon nanotube pillar array on field-emission properties. *Jpn. J. Appl. Phys.* 55:06GF12
- Wei Z, Mahadevan L. 2014. Continuum dynamics of elastocapillary coalescence and arrest. *Europhys. Lett.* 106:14002
- Weijss JH, Andreotti B, Snoeijer JH. 2013. Elasto-capillarity at the nanoscale: on the coupling between elasticity and surface energy in soft solids. *Soft Matter* 9:8494–503
- Weijss JH, Snoeijer JH, Andreotti B. 2014. Capillarity of soft amorphous solids: a microscopic model for surface stress. *Phys. Rev. E* 89:042408

- Wexler JS, Heard TM, Stone HA. 2014. Capillary bridges between soft substrates. *Phys. Rev. Lett.* 112:066102
- Xuan C, Biggins J. 2016. Finite-wavelength surface-tension-driven instabilities in soft solids, including instability in a cylindrical channel through an elastic solid. *Phys. Rev. E* 94:023107
- Zell ZA, Choi SQ, Leal LG, Squires TM. 2010. Microfabricated deflection tensiometers for insoluble surfactants. *Appl. Phys. Lett.* 97:133505
- Zhao YP, Fan JG. 2006. Clusters of bundled nanorods in nanocarpet effect. *Appl. Phys. Lett.* 88:103123

Contents

John Leask Lumley: Whither Turbulence? <i>Sidney Leibovich and Zellman Warhaft</i>	1
Agitation, Mixing, and Transfers Induced by Bubbles <i>Frédéric Rissio</i>	25
Numerical Models of Surface Tension <i>Stéphane Popinet</i>	49
Some Recent Developments in Turbulence Closure Modeling <i>Paul A. Durbin</i>	77
Diffuse-Interface Capturing Methods for Compressible Two-Phase Flows <i>Richard Saurel and Carlos Pantano</i>	105
Instabilities of Internal Gravity Wave Beams <i>Thierry Dauxois, Sylvain Joubaud, Philippe Odier, and Antoine Venaille</i>	131
Hydraulic Mineral Waste Transport and Storage <i>Lionel Pullum, David V. Boger, and Fiona Sofra</i>	157
Fire Whirls <i>Ali Tobidi, Michael J. Gollner, and Huabua Xiao</i>	187
High Explosive Detonation–Confiner Interactions <i>Mark Short and James J. Quirk</i>	215
Slamming: Recent Progress in the Evaluation of Impact Pressures <i>Frédéric Dias and Jean-Michel Ghidaglia</i>	243
Double-Diffusive Convection at Low Prandtl Number <i>Pascale Garaud</i>	275
Microstructural Dynamics and Rheology of Suspensions of Rigid Fibers <i>Jason E. Butler and Braden Snook</i>	299
Nonlinear Nonmodal Stability Theory <i>R.R. Kerswell</i>	319
Intracellular Fluid Mechanics: Coupling Cytoplasmic Flow with Active Cytoskeletal Gel <i>Alex Mogilner and Angelika Manhart</i>	347

Active and Passive Microrheology: Theory and Simulation <i>Roseanna N. Zia</i>	371
Particle Segregation in Dense Granular Flows <i>John Mark Nicholas Timm Gray</i>	407
The Sound of Flow Over Rigid Walls <i>William Devenport, Nathan Alexander, Stewart Glegg, and Meng Wang</i>	435
Lymphatic System Flows <i>James E. Moore Jr. and Christopher D. Bertram</i>	459
Microfluidics to Mimic Blood Flow in Health and Disease <i>Bernhard Sebastian and Petra S. Dittrich</i>	483
Hydrodynamic Interactions Among Bubbles, Drops, and Particles in Non-Newtonian Liquids <i>R. Zenit and J.J. Feng</i>	505
Wall-Modeled Large-Eddy Simulation for Complex Turbulent Flows <i>Sanjeeb T. Bose and George Ilhwan Park</i>	535
Rheology of Active Fluids <i>David Saintillan</i>	563
Supersonic Combustion in Air-Breathing Propulsion Systems for Hypersonic Flight <i>Javier Urzay</i>	593
Elastocapillarity: When Surface Tension Deforms Elastic Solids <i>José Bico, Étienne Reyssat, and Benoît Roman</i>	629
Sensitivity and Nonlinearity of Thermoacoustic Oscillations <i>Matthew P. Juniper and R.I. Sujith</i>	661
Instabilities in Blistering <i>Anne Juel, Draga Pihler-Puzović, and Matthias Heil</i>	691

Indexes

Cumulative Index of Contributing Authors, Volumes 1–50	715
Cumulative Index of Article Titles, Volumes 1–50	725

Errata

An online log of corrections to *Annual Review of Fluid Mechanics* articles may be found at <http://www.annualreviews.org/errata/fluid>